RETRIEVAL OF A HIGH RESOLUTION DEM FROM UAV PHOTOGRAMMETRY FOR DEFINING THE FLOOD WATER LEVEL EXTENTS DETECTED WITH SAR IMAGES

HARIADY INDRA MANTONG
March, 2018

SUPERVISORS:
Dr. Ir. C. van der Tol
Ir. G.N. Parodi

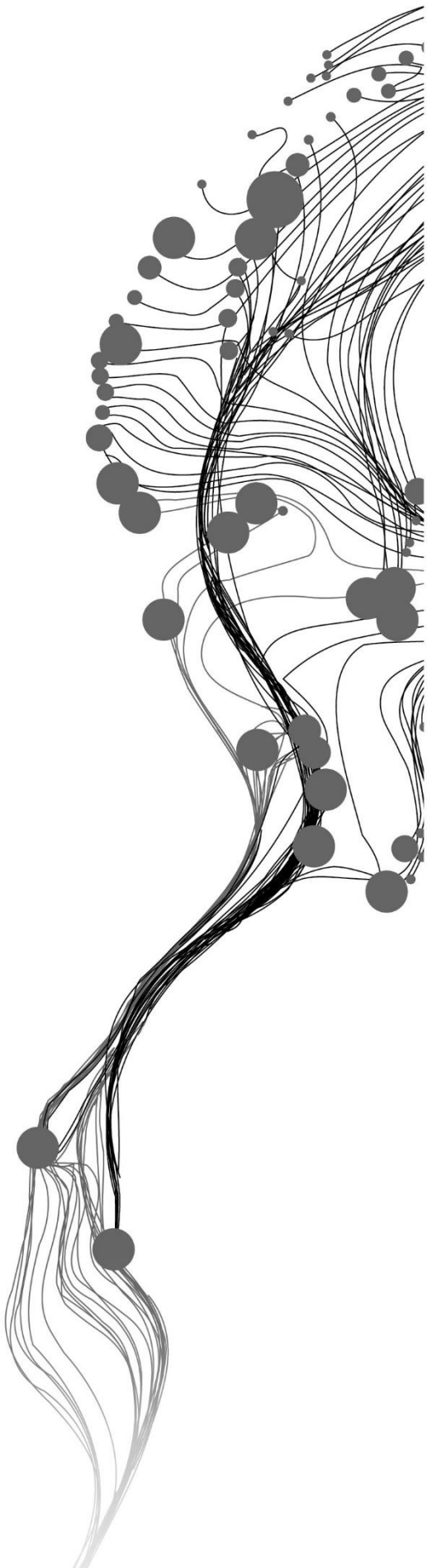

RETRIEVAL OF A HIGH RESOLUTION DEM FROM UAV PHOTOGRAMMETRY FOR DEFINING THE FLOOD WATER LEVEL EXTENTS DETECTED WITH SAR IMAGES

HARIADY INDRA MANTONG

Enschede, The Netherlands, March, 2018

Thesis submitted to the Faculty of Geo-Information Science and Earth Observation of the University of Twente in partial fulfilment of the requirements for the degree of Master of Science in Geo-information Science and Earth Observation.
Specialization: Water Resources and Environmental Management

SUPERVISORS:
Dr. Ir. C. van der Tol
Ir. G.N. Parodi

THESIS ASSESSMENT BOARD:
Dr.ing. T.H.M. Rientjes (Chair)
Dr. F.C. Nex (External Examiner, ITC, University of Twente)

DISCLAIMER

This document describes work undertaken as part of a programme of study at the Faculty of Geo-Information Science and Earth Observation of the University of Twente. All views and opinions expressed therein remain the sole responsibility of the author, and do not necessarily represent those of the Faculty.

ABSTRACT

In recent times, the utilization of Unmanned Aerial Vehicle (UAV) as known as drone has become an important platform for remote sensing and digital photogrammetry. The UAV has been effectively used for image acquisition from low altitude flight to produce a high-resolution image. This high-resolution images form a surface terrain information as Digital Surface Model (DSM) based on the features matching algorithm of the overlapping images. The features matching of the overlapped images construct dense-matching point clouds and generate DSM. As a surface model, DSM does not represent a real terrain platform. Then, the reliability of the DEM generated from UAV to be used as the terrain platform for hydraulics modeling remains questionable. Therefore, it requires to be converted to Digital Elevation Model (DEM) to be used as the main parameter. The main objective of the research is to investigate the reliability of DEM retrieved from UAV for hydraulics modeling purposes.

This study generated four sets of DEM; two DEMs with different grid resolution: 2cm and 40cm and two other DEMs with different ground filtering algorithm: extra fine nature and filtering parameter (bulge, offset, spike, and standard deviation) customizations. The reliability of these sets generated DEMs as the terrain representation was investigated by validating the DEMs with the reference points from the terrestrial measurement. The reference points were measured from The RTK-GPS method with 20mm accuracies in vertical direction, which considered as an accurate reference. The validation of UAV's DEMs that were generated from ground filtering parameters modification showed the highest correlation with the reference terrain. The Root Mean Square Error (RMSE) from the comparison between ground filtering parameters modification DEM with the reference terrain showed the smallest errors: RMSE 6.17 cm for 2cm resolution and 5.22 cm for 40cm resolution.

As the indication of UAV's DEM reliability in hydraulic modelling application, the generated DEMs were used as the terrain platform to estimate the flood water level extent based on the flood detected by SAR images. Then, it applied the flood detection with SAR images resulted in 46 flood images from Sentinel-1 images observations captured in October 2014 to December 2017. These 46 flood images were overlaid with the UAV's DEM to retrieve the flood water level at the observed inundated area. The method of this water level measurement has successfully produced a water level estimation values. This water level values were later validated with the water level values from the in-situ measurement, resulting in comparable result of correlation and the RMSE value of 6,72 cm for DEM 40cm resolution application. This study showed a reliable result for UAV's DEM application to estimate the flood water level. Based on the research result, indicated that the application of UAV's DEM platform as the main parameter in hydraulic modelling is reasonable.

Keywords: DEM retrieved from UAV, Hydraulics modelling, SAR images, UAV photogrammetry, Water Level Estimation

ACKNOWLEDGEMENTS

All praise, honour and glory to my Lord Jesus Christ for His richest grace and faithfulness in completing my master degree.

I would like to express my earnest gratitude to Netherland Fellowship Programme (NFP) Scholarship for providing me with an exquisite opportunity to chasing my dream and ambitions

I would like to express my sincere gratitude to my supervisors: Dr. Ir. C. van der Tol and Ir. G.N. Parodi for their advice, encouragement, guidance, and constructive critics of this research work

My special thanks to my colleagues Rebecca Addae and Firaol Befekadu for the thoughts, advice and technical supports to improve the thesis. I also owe my incredible thanks to all of my classmates from WREM Master of Science Programme and my fellow Indonesian for the supports and encouragement during the programme to the completion of the thesis.

I am forever so much grateful to have my wife, children, parents, family and friends who always encouraged and prayed for me throughout the time of my study and research.

This thesis is heartily dedicated to my mother who took the lead to heaven before the completion of this work.

TABLE OF CONTENTS

List of figures iv
List of tables iv
1. INTRODUCTION 1
1.1. Background 1
1.2. Problem Statement 3
1.3. Research Objectives 3
1.4. Research Question 3
1.5. Study Area 4
2. RESEARCH METHOD 6
2.1. Produce a protocol of DEM generation from UAV for Hydraulics Modeling Purposes 7
2.1.1. UAV's Image Acquisition 7
2.1.2. Image Processing 8
2.1.3. Quality analysis of image processing 10
2.1.4. Terrestrial Measurement for UAV's DEM Validation Purpose 11
2.1.5. Conversion of UAV's Digital Surface Model (DSM) to Digital Elevation Model (DEM) 13
2.2. Examine the accuracy of DEM from UAV 20
2.2.1. Generate high accuracy DEM 20
2.2.1. Validation of UAV's DEM with DTM from Terrestrial Measurement 20
2.3. Application of UAV's DEM and SAR Imagery Observation for water levels and flood extents estimation 21
2.3.1. Pre-processing of SAR Images 21
2.3.2. Image Classification for Flood Extent Retrieval 22
2.3.3. Water Levels Retrieval from Classified Image with UAV's DEM as the platform 25
3. RESULTS 31
3.1. UAV's Image Acquisition and Processing 31
3.2. DSM to DEM Conversion 33
3.3. Flood Extent Threshold Determination from multi-temporal SAR imagery on the UAV's DEM platform 38
4. DISCUSSION 43
4.1. DEM Generation from dense-matched points of UAV Imagery 43
4.2. Assessment Accuracy of UAV's DEM generated 45
4.3. Flood Water Level Determination from SAR Imagery 45
5. CONCLUSION 47
5.1. Limitations 47
5.2. Recommendation 48
LIST OF REFERENCES 49

LIST OF FIGURES

Figure 1. 1. The Difference between Surface Model and Terrain Model 2
Figure 1. 2. Conversion from DSM to DEM 2
Figure 1. 3. Area of Study 4
Figure 2. 1. Research Flowchart 6
Figure 2. 2. Flight plan and UAV type used 7
Figure 2. 3. Image Processing Flowchart 8
Figure 2. 4. Ground Control Points (GCP) features 8
Figure 2. 5. Initial Image Position 9
Figure 2. 6. Quality Report Rubrics 10
Figure 2. 7. Initial Processing General Summary 10
Figure 2. 8. Summary of Point Cloud Densification 11
Figure 2. 9. RTK-GPS Measurement Concept. Source: (Van Sickle, 2001) 12
Figure 2. 10. RTK GPS Instrument, Smartworx Viva Interface, and Field Measurement 12
Figure 2. 11. Distribution of The Reference Points and The Measurement Process 13
Figure 2. 12. DSM to DEM Conversion Steps 14
Figure 2. 13. Noise Inspection at DSM LAS file 15
Figure 2. 14. Comparison before and after noise removed 15
Figure 2. 15. Re-tiling Process 16
Figure 2. 16. Report of LAS file sorting 16
Figure 2. 17. Sub-tile Noise Inspection 17
Figure 2. 18. Report of Ground Class Extraction with **Extra Fine Nature** 18
Figure 2. 19. Report of Ground Class Extraction with **Filtering Parameter Modification** 18
Figure 2. 20. Report of Conversion to DEM **to Extra Fine Nature Ground** 19
Figure 2. 21. Report of Conversion to DEM to **Filtering Parameters Modification Ground** 19
Figure 2. 22. Pre-processing: Terrain Correction, Subseting, and Filtering 22
Figure 2. 23. Visual Comparation of VH and VV Polarization on Flooding Monitoring from Sentinel-1 images 23
Figure 2. 24. Comparison on Image Filtering of Sentinel-1 Images 24
Figure 2. 25. Stacking and Overlay on Sentinel-1 Images 25
Figure 2. 26. The Sentinel-1 Images Stacked from Dry and Flooded Event 26
Figure 2. 27. Field Work Documentation when The Area was Dry and when it was Flooded 26
Figure 2. 28. RGB Colour Composite Formation 27
Figure 2. 29. Result of Colour Composite Image from Dry and Flooded Image 27
Figure 2. 30. Backscatter Value Determination for Flooded Pixel 28
Figure 2. 31. Sentinel-1 Flooded Images with Ascending and Descending Pass 28
Figure 2. 32. Flood Maps Generation Process in Batch Processing 29
Figure 2. 33. Water Level Estimation from SAR Images Flood Map 29
Figure 3. 1. Offset between Initial and Computed, Keypoints Matches Link, and Number of Overlapping Images 32
Figure 3. 2. Image Processing Results : i) Point clouds, ii) DSM in LAS file format, iii) Orthophoto 33
Figure 3. 3. RTK GPS Points Distribution 36
Figure 3. 4. Validation of Elevation Models at the Reference Points 37
Figure 3. 5. Flood Frequency Map based on Flood Detection on SAR Imagery October 2017 to December 2017 40
Figure 3. 6. Accuracy Assesment of generated DEM application for flood water level estimation 42

LIST OF TABLES

Table 3. 1. GCPs Accuracies in Images Georeferencing Process 31
Table 3. 2. Comparison on 2cm Accuracy of the Generated DEM and DSM 34
Table 3. 3. Comparison on 40 cm Accuracy of Generated DEM and DSM 35
Table 3. 4. RMSE Values of Elevation Models to Reference Points 38
Table 3. 5. The list of 46 Flooded Images from December 2014 to December 2017 39
Table 3. 6. Water Level Measurement from SAR Images Flood Maps and In-situ Measurement 41
Table 3. 7. Water Level Measurement at Zoekerbrug Station 42
Table 3. 8. RMS Errors of Water Level from UAV's DEM and DEM AHN2 compared with In-situ Measurement 42

1. INTRODUCTION

1.1. Background

Topography representation is a main parameter for earth science applications; geophysics, ecology, geology, geomorphology, polar studies, and hydrology (Jenson, 1991). Water flow at the surface and in the subsurface is determined by gravitational potential and directly influenced by morphology (Drever, 2005; Dunne & Black, 1970). Surface terrain is taken into account to develop physically based models of hydrological processes due to inherent relationship between downstream flow and surface relief within the watershed (Woodrow, Lindsay, & Berg, 2016). An extensive range of recent modeling studies has simulated the flow directions and volumes driven by hydraulic gradients, derived from surface topography (Altenau et al., 2017; Ullah et al., 2016; Judi, Burian, & McPherson, 2011; Remo, Carlson, & Pinter, 2011). The terrain attribute of the model needs to be well parameterized to minimize uncertainties that will affect the model accuracy (Mukolwe, Baldassarre, Werner, & Solomatine, 2014). Terrain attribute as the main parameter is quantified from an ordered array of numbers that represent the spatial distribution of elevations above a datum over a specified segment of the landscape (Moore, Grayson, & Ladson, 1991). Noticed of how major the terrain parameter in hydraulic modeling is, there are methods which are developed to obtain accurate data of the surface terrain.

Terrain survey and analysis have been done by conventional (geodetic) techniques as well as remote sensing methods. Terrain information which is generated from these techniques formed in digital labelled as Digital Elevation Models (DEM). DEM resolution has a significant effect on the result of 1D or 2D hydraulic model (Haile & Rientjes, 2005). Therefore, to obtain a reliable hydraulic model result, high-resolution DEMs are required. The geodetic method provides high accuracy and precision, but it is time-consuming (Uysal, Toprak, & Polat, 2015). However, rapid development of remote sensing technologies offers efficiency in terrain parameter retrieval equipped with good accuracy (Chen, Li, Yan, Dai, & Liu, 2015). A breakthrough innovation in photogrammetry had delivered Airborne Light Detection and Ranging (LiDAR) with high horizontal and vertical accuracy. The high density of point cloud from LiDAR produces more precise DEMs, up to 25 cm (depend on the sensor) that ideally reliable for Hydrologically Sensitive Areas (HSAs) delineation (Thomas et al., 2017). Even though it is reliable, LiDAR is considered very costly and relatively time consumed for a small area due to airborne flight preparation needs and regulations that might strict in some areas.

In recent times the utilization of Unmanned Aerial Vehicle (UAV) as known as drone has become an important platform in remote sensing and digital photogrammetry (Tamminga, Hugenholtz, Eaton, & Lapointe, 2015). In the relatively small area, using UAV has been proven effectively capture the detailed land cover from low altitude and produce a high-resolution image (Hua, Qi, Shang, Hu, & Han, 2016). The UAV application has demonstrated the possibility to create a DEM with less than 20 mm height uncertainty over a flat, open, and gravel area of 0.6 ha at 160 m flight height and as low as 10 mm height uncertainty at flight height about 80 m (Reshetyuk & Mårtensson, 2016). Hence, UAVs are practically useful for a high accurate of DEMs generation, therefore improving cost efficiency of surveying work.

DEM represents the geometrical features that aid in the characterization of the watershed boundary condition while other geospatial information defines hydraulical parameters, such as roughness, ponding, structures, and barriers (Zhang et al., 2014). The extraction of geometric representation from aerial imagery is based on features matching algorithm of the overlapping images that generate multi-view stereo image matching (Haala & Cavegn, 2016). UAV captures the earth morphology and produces the surface terrain information as Digital Surface Model (DSM). In principal, as shown in Figure 1.1 DSM provides the

elevation of natural and human-made features while for hydraulic modeling, the elevation used is DEM (Reshetyuk & Mårtensson, 2016).

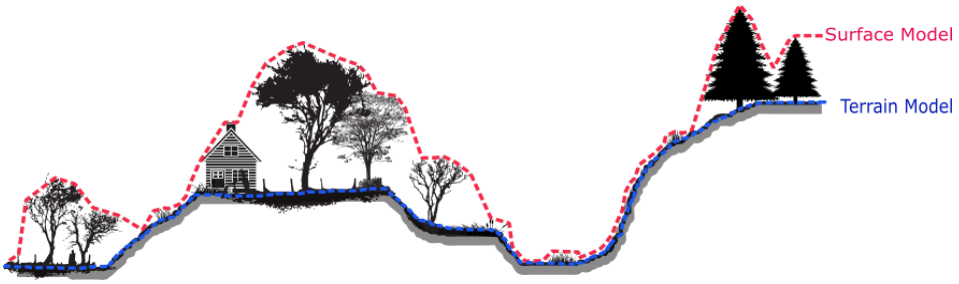

Figure 1. 1. The Difference between Surface Model and Terrain Model

The quality of DEM retrieved will determine how hydraulic model works successfully. The variables, parameters and technical processes that used in generating DEM from UAV have different effects on the DEM accuracy. Therefore, investigation on the method of DSM to DEM conversion (Figure 1.2) from UAV photogrammetry needs to be emphasized to be able to produce a reliable result.

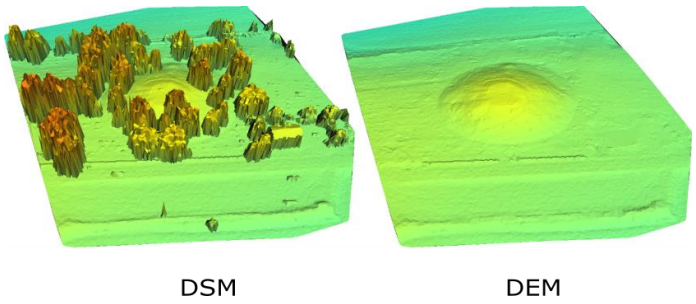

Figure 1. 2. Conversion from DSM to DEM
(Source: Smith, 2015)

As terrain functioned to be a major parameter, hydraulics modeling also required a temporal trustworthy observation data in term of flood extent extraction and water level estimation (Hostache et al., 2009). This information retrieved traditionally from gauging in-situ measurement of water level and discharge on the field and have been using for modeling. However, the increasing availability of remote sensing-derived (RS-D) utilization of flood extent and the water level have been effectively offering a comprehensive analysis of hydraulic models forecast capability (Grimaldi, Li, Pauwels, & Walker, 2016).

Active microwave satellite imagery of synthetic aperture radar (SAR) has deemed as the most reliable information source for inundated area delimitation, flood monitoring and forecasting (Di Baldassarre et al., 2009; Stephens et al., 2012; Greifeneder et al., 2014; Schumann & Moller, 2015; Tanguy et al., 2017). SAR images retrieve the values of water bodies and the flood extent extraction. These values are forming the flooded-inundated area constraints and merge with the DEM as the platform parameter to apply the objective protocols as hydraulic coherence (Hostache et al., 2009). The availability of in-situ gauging measurement data of water level and river discharge effectively used for hydraulic model calibration and validation to increase the accuracy and precision of flood forecast (Grimaldi et al., 2016). Furthermore, integration of SAR imagery application with gauging field measurement data and DEM retrieved from UAV were addressed in this research.

1.2. Problem Statement

The problem is UAV generates the terrain information as Digital Surface Model (DSM) from the nadir view images where features captured from this point of view were the surfaces of natural and man-made objects. While hydraulic models purposes necessitate a very low height uncertainty and accurate slope geometric of the ground. The accuracy of UAV to extract and represents the geometric dimension might be different on land covers and terrains types. A DSM can be converted to a DEM based on interpolation method, in which different parameters are considered that affect the quality of the generated ground surface. An accurate DEM requires well-structured processes started from a high-density point cloud generation which characterized the surface accurately and is determined by the precision of photogrammetry image processing. There is none specific parameter setup which means by default that will determine the accuracy of the generated DEM. Therefore the best approach to produce valid terrain information is by trial and error with customization of the involved parameters. Every different setup value will give certain influence to the generated terrain. These have been challenging for the use of UAV to retrieve a high accuracy elevation model that is adequate for hydraulic modeling. This terrain information will be later assessed visually and numerically so there will be one parameter set which fit the best for the area.

As the platform for hydraulics model, the DEM needs to be validated with hydrodynamics observation data. The flood extent, water level, and inundated area of the river plane can be well observed from remote sensing products, particularly from SAR imagery. Retrieving the information from SAR images is not straightforward, it needs correct interpretation to avoid inaccuracies of the outcomes. SAR temporal series observations on the flooded area yield the historical hydrodynamics information as polygons. Being quantified in the polygons means that the size of the impacted area can be measured and the water level when it is flooded can be estimated. Either the size of the inundated area or the flood water level can be measured using the terrain platform. However, the reliability of the DEM generated from UAV to be used as the terrain platform for flood water level estimation are still required to be investigated. This investigation on UAV's DEM application for water level and flood extent estimation is addressed in this research. Further, the investigation is expected to produce recommendations of UAV's DEM applications for hydraulics modeling purposes.

1.3. Research Objectives

The main objective of the research is to investigate the reliability of DEM retrieved from UAV for hydraulics modeling purposes. This goal will be achieved after a number of secondary objectives:

i. To generate a robust protocol for DEM generation from UAV
ii. To examine the accuracy of the retrieved UAV's DEM
iii. To determine flood extent threshold from the water bodies extraction of multi-temporal SAR imagery on the UAV's DEM platform.

1.4. Research Question

To achieved the objectives stated, the following questions are addressed:

For Secondary Objective 1

- What are the effects of numbers and distributions of GCP's to the UAV's image orientation and the point cloud density of DSM generated?
- What are the required process steps to generate DEM from UAV?

For Secondary Objective 2

- What is the accuracy of the DEM generated?

For Secondary Objective 3

- What is the estimated water level at flood event detected with SAR imagery, measured from the UAV's DEM platform generated?
- What is the relation between the water level from in-situ measurements with water level measured from the UAV's DEM generated?
- Which relevant information can be obtained from the water level estimation method that applied in this research for flood detection and management in the future?

1.5. Study Area

The study area selected for the research is a part of the Dinkel River floodplain which is located in the eastern part of Province Overijssel, the Netherlands. The Dinkel River originates from North Rhine-Westphalia, Germany, flows to Gronau, crosses the border with the Netherlands through Losser, Denekamp, and flows back to Germany at Lower Saxony. The Dinkel is a meandering sand-bed river with undulating topography, underlain mainly by cretaceous limestones, tertiary clays and pleistocene tills. The land use at the plain along Dinkel River is mainly a farming land for dairy, while approximately 10% of the area was stated as nature conservation in European Natura 2000 policy.

The landforms in the River Dinkel valley have been formed by channel migration, meander cutoffs and overbank deposition processes which have been active at least throughout the last 150 years (Wolfert, 2001). The rehabilitation at the river geomorphological as part of the water management has resulted in a shorter route channel, which implies a sudden increase in water gradient and stream power. Most of the floodplains along the Dinkel River have been re-restored particularly as a flood prevention and environmental improvement program by the government, under the authority of regional *Waterschap* (Waterboard). Some parts of the river valley have been used for water retention as new inundation zones as creation of man-made natural floodplain areas. These natural man-made floodplains were generally inundated during winter time due to large volumes of runoff discharge and rising water level combined with undulating topography and impermeable subsoil, while in the summer the baseflow discharge occurred.

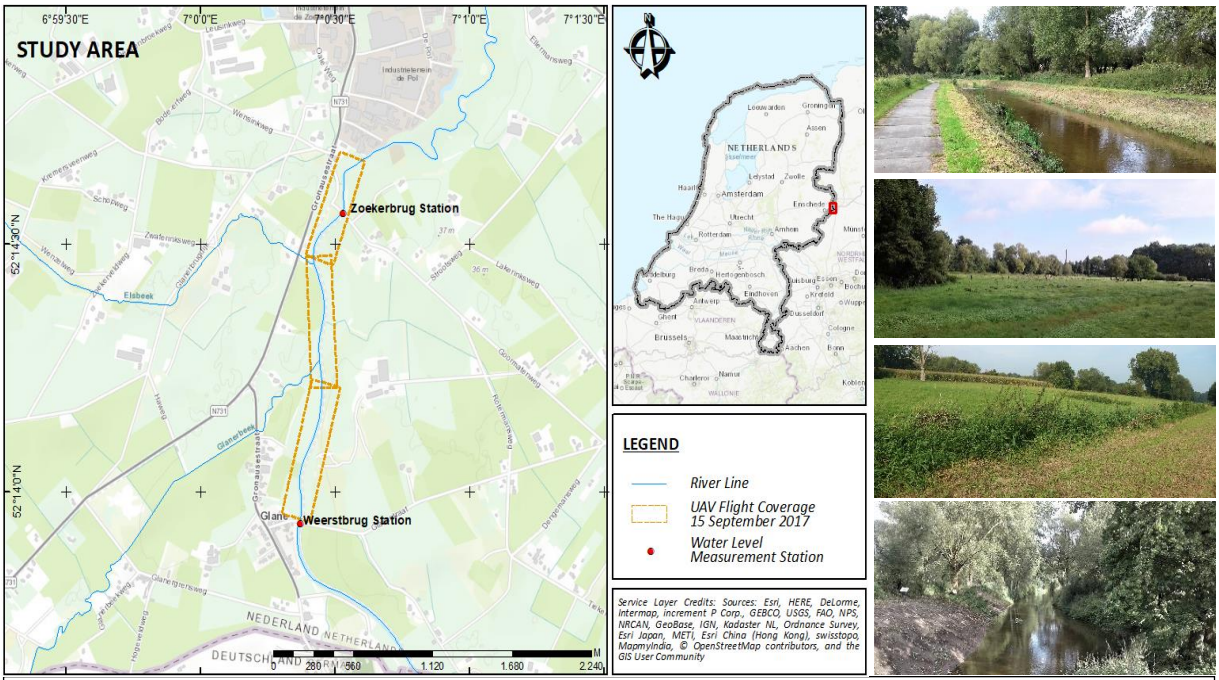

Area of Study is the river section between Glane and Losser at the east part of Overijssel Province, The Netherlands . Covered two water level in-situ measurement station at UAV Image acquisition on 15 September 2017 as documented with the fieldwork photos of the area.

Figure 1. 3. Area of Study

The area of study as shown in Figure 1.3 is the first section of the Upper Dinkel River in The Dutch side. The study area is a section of about 2 km length along the Dinkel River, from Weertsbrug water level measurement station to the Zoekerburg station. The site is the floodplain area at the man-made canal between Glane and Losser. There are two tributary channels to this river section, which are Glanerbeek and Elsbeek. At a certain time in the early winter, there is frequently over-bank water flows at this river section which was routinely observed from the water level stations at the section. In this particular time, high discharge of the river experiences inundation in flood plains and the observation area.

The type of land covers in the area is varied with grass, farming pasturage, maize, bushes, dense trees, dairy farm, and houses. This land cover variety captured in the UAV images and affect differently in the quality of DSM generated, based on the feature matching processing that mainly contributes to the point cloud density. This is the main reason why the variety of land cover and terrain type required to be captured in the image acquisition. However, UAV flight and terrestrial measurement in the area required consideration of aviation regulation from the government in the form of a no-fly zone for drones, protected habitats directive of Natura 2000, and permission from the residents.

2. RESEARCH METHOD

The method of the research is illustrated in a flowchart Figure 2.1 based on research objectives that was applied in three domains:

1. Produce a protocol of DEM generation from UAV
2. Examine the accuracy of DEM retrieved from UAV
3. Determine flood extent threshold from the water bodies extraction of multi-temporal SAR imagery on the UAV's DEM platform.

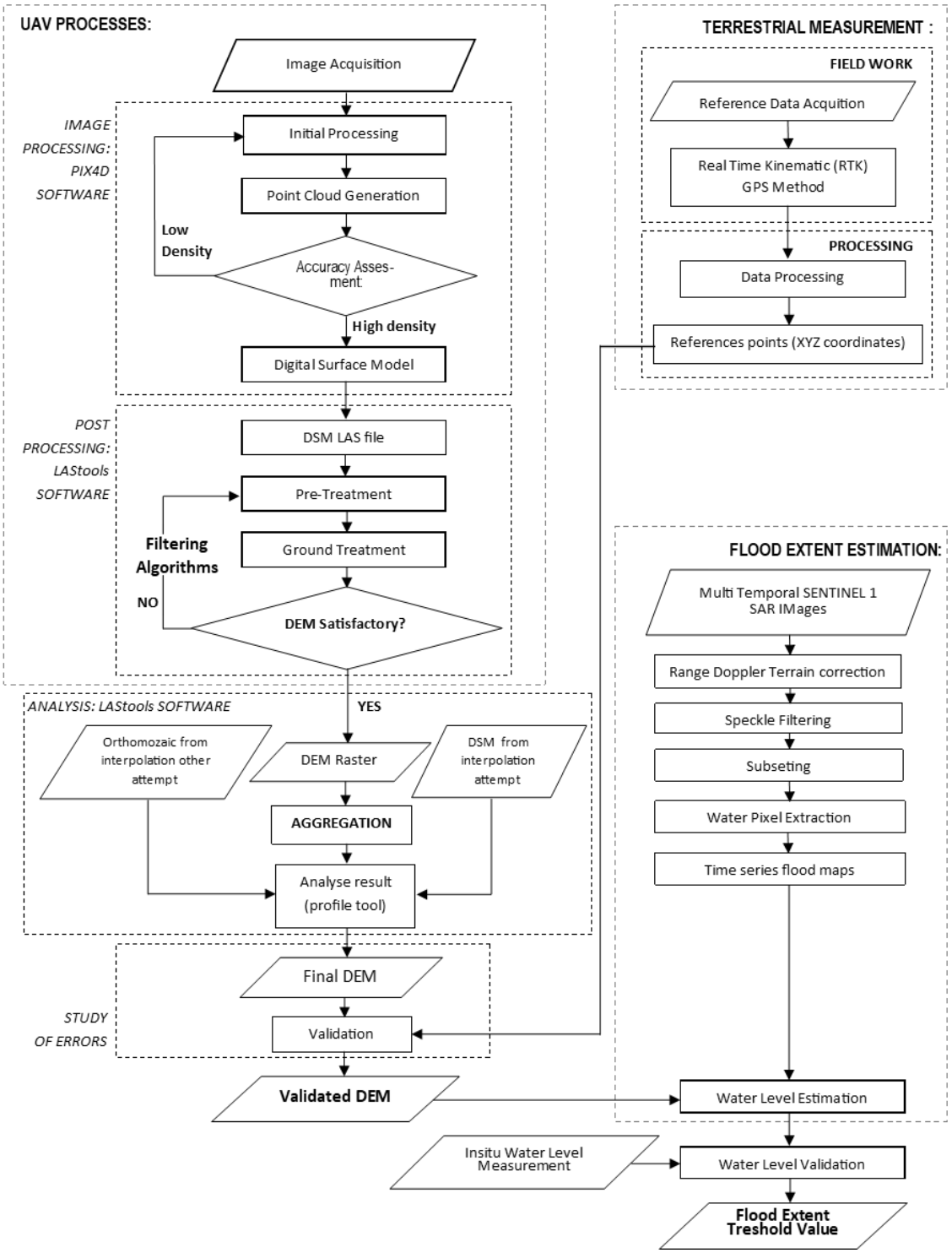

Figure 2. 1. Research Flowchart

2.1. Produce a protocol of DEM generation from UAV for Hydraulics Modeling Purposes

First, the protocol was designed to carry out the DEM from UAV. The protocol of DEM retrieval from UAV for the research was broken down into five process steps: UAV's image acquisition, image processing, quality analysis of image processing, terrestrial topographic measurement as the reference data, and conversion of UAV's DSM to DEM as outlined in Section 2.1.1 to 2.1.5 below.

2.1.1. UAV's Image Acquisition

This procedure was crucial to obtain a primary data for the research. It needs to be done properly based on the expected DEM's accuracy. This photogrammetry process was the first step applied to have a high density of points cloud data. The image acquisition process started from designing the flight plan that fits the research objectives. In principle, low altitude flight results the higher spatial resolution of images and vice versa. On the other hand, effective image acquisition plan should consider the type of land cover, and the terrain of the captured area. A high-density object such as dense vegetation and forest affects differently to be captured by moving sensor with certain flight altitude compare to low-density objects. The dense and similar objects like vegetation's leaves were difficult to be captured with an exact shape in the consecutive images from the low altitude of moving flights, due to wind effect that makes the object also move dynamically. This is why the image acquisition plan needs to be done after the preview observation to the area.

The UAV type used for the research was the DJI Phantom 4, operated with *pix4d mapper capture* app (Figure 2.2). The acquisition was completed on three flight missions that covered the area along the river. The vehicle's camera used a focal length that corresponds to the 35mm equivalent and flew at 50 meters altitude with 80% forward overlap and 80% side overlap. The camera's focal length and the flight altitude were considered to have a certain Ground Sampling Distance (GSD) which was 2cm in this images acquired. GSD of 2cm represents linearly 2cm x 2cm equal to 4cm² on the ground.

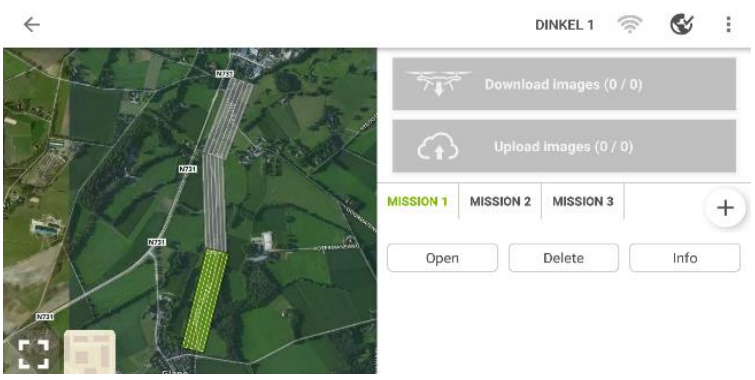

Three flights missions that were planned on the research area, UAV flights started from mission 1 (green dots) to the last flight of mission 3.

Quadcopter UAV used for the research: DJI Phantom 4 and the controller.

Figure 2. 2. Flight plan and UAV type used

In the image acquisition process, a numbers of Ground Control Point (GCP) have been distributed in the area. GCPs in this process were functioned as reference points for the orientation/georeferencing of the images. The GCPs were placed/stated at before and after the flights, using a natural and artificial object that was clearly recognised from the images. The GCP's were measured using RTK-GPS Method with the terrestrial instrument Leica CS15 Viva Field Controller and GS14 RTK GNSS GPS Bluetooth Smart Antenna. The manufactured accuracy for RTK Network is 8mm + 0.5 ppm (rms) Horizontal and 15mm + 0.5 ppm (rms) Vertical (Leica, 2018).

2.1.2. Image Processing

Every process that has been applied in this image processing was aimed to generate a high-density point cloud for the Digital Surface Model (DSM) formation. The dense point cloud determined the actual reconstruction of DSM and later affected the accuracy of generated terrain model compared with the real topography. Semi-automatically photogrammetry procedure was operated in this research, using the digital photogrammetry *pix4d mapper* software.

There were three main steps of image processing that have been done; (1) initial processing, (2) point cloud densification-mesh generation, and (3) DSM-Orthophoto construction. The steps were applied in particular order as elaborated in Figure 2.3 below.

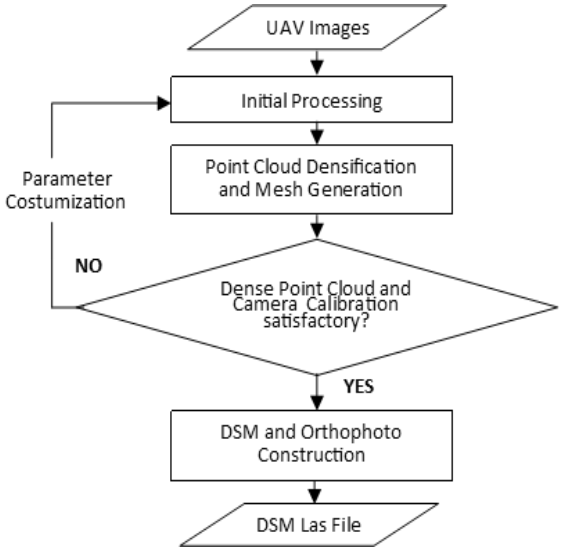

Figure 2. 3. Image Processing Flowchart

In the initial processing, the UAV retrieved images were processed for the key points extraction to have feature matching from all consecutive images. Largely matching of one image to another is the key for the accurate surface reconstruction of the area. Image matched process was started with georeferenced using the GCPs as the reference points. Image georeferenced applied to give the orientation to the images based on one particular world projection system. The GCPs that were used for this image georeference are the recognisable surface's features on the images as illustrated in Figure 2.4 below.

GCPs were chosen from the man-created objects on the ground that clearly recognized from the image. GCPs were measured on the field with RTK differential GPS instrument.

Figure 2. 4. Ground Control Points (GCP) features

The GCP's features in the images above were manually noticed and marked on each overlapped images. These GCPs has fixed position on the ground, were not moved or moving since it was terrestrially measured until it tied on the images. These points were used as georeferenced tie points for the bundle block images orientation as seen in Figure 2.5 below.

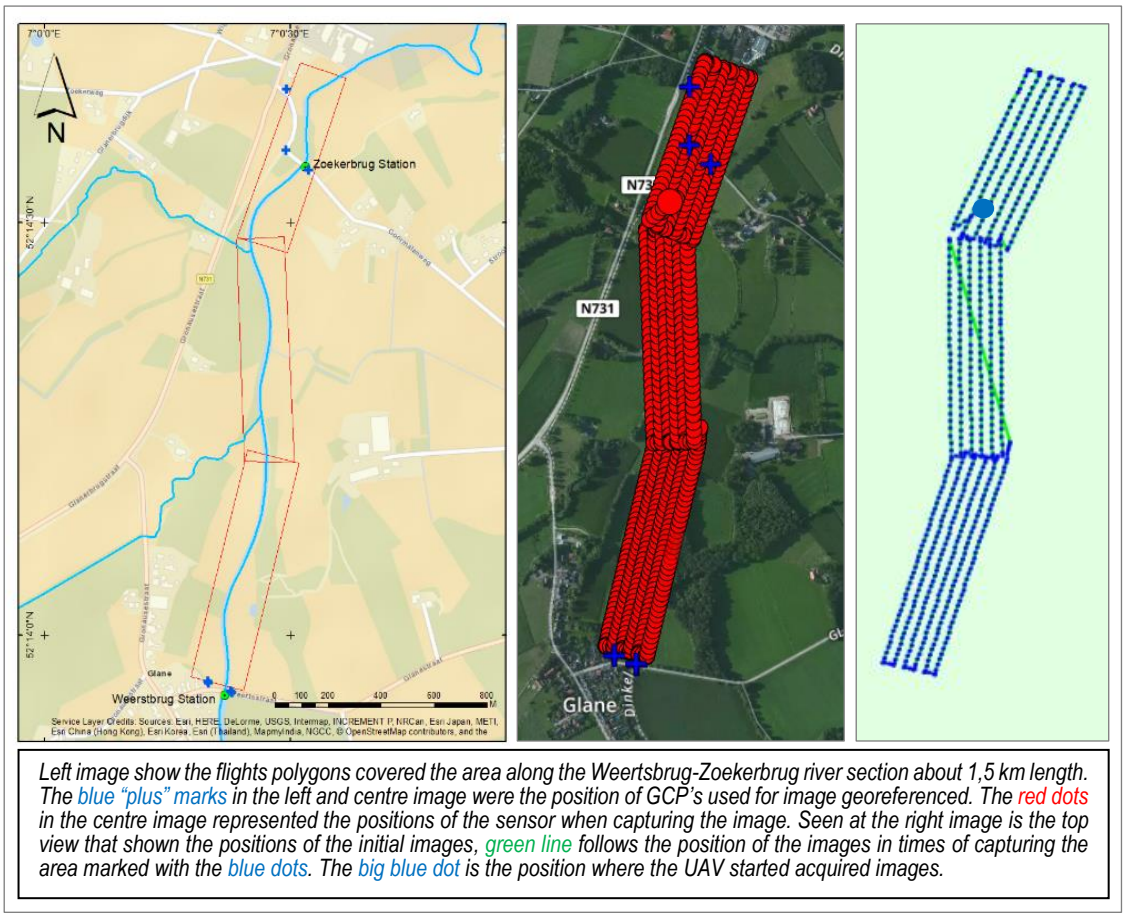

Left image show the flights polygons covered the area along the Weertsbrug-Zoekerbrug river section about 1,5 km length. The blue "plus" marks in the left and centre image were the position of GCP's used for image georeferenced. The red dots in the centre image represented the positions of the sensor when capturing the image. Seen at the right image is the top view that shown the positions of the initial images, green line follows the position of the images in times of capturing the area marked with the blue dots. The big blue dot is the position where the UAV started acquired images.

Figure 2. 5. Initial Image Position

The image georeferenced was demonstrated acceptable accuracy (result, Table 3.1) for further application. The evenly distributed GCPs were given a very constructive influence to the image block orientation as indicated from the RMSE value (Figure 2.6), even though adding few more GCPs at around the middle part of the area equally were still needed. It is crucial to consistently plot the GCP's evenly distributed on the area following the "shape" of the polygon's area of interest.

After the georeference, the image block was processed to generate the first ray cloud. This ray cloud showed the quality of initial image processing, indicated that this cloud needs to be increased to retrieve more dense point cloud for the proper DSM product. Then, the point cloud was densified with customization on image scale, point density optimisation, and numbers of least images that reprojected correctly. Adjustment of these three parameters needs to consider the computer specification support, especially the RAM capacity. The bigger the image scale, point density, and a minimum number of matched images, the longer the processing time. The point cloud improvement required to be applied in the image processing as it is the primary data for retrieving the real terrain. This is the main reason for the point cloud densification which applied multiple times. Dense point cloud affected the mesh quality as a surfaces representation of the captured area. The mesh results were further processed to generate the DSM, and later to converted to DSM LAS File.

2.1.3. Quality analysis of image processing

Every part of the image processing is assessed and exposed in a report. As the initial processing result presented as the ray cloud, there are numbers of quality check rubrics in Figure 2.6 below: the amount of matched key points as well as matched images, numbers of calibrated images, camera parameters optimisation result, and the accuracy of georeferencing with the Root Mean Square Error (RMSE) value.

Quality Check

Images	median of 48109 keypoints per image	✓
Dataset	677 out of 677 images calibrated (100%), 6 images disabled	✓
Camera Optimization	2.03% relative difference between initial and optimized internal camera parameters	✓
Matching	median of 10746.2 matches per calibrated image	✓
Georeferencing	yes, 7 GCPs (7 3D), mean RMS error = 0.033 m	✓

Figure 2. 6. Quality Report Rubrics

As shown in Figure 2.6 above, all the rubrics were checked signified that result on every rubric is acceptable. The initial processing itself was reported in the overview summary as shown in Figure 2.7 below.

Initial Processing Summary :

Project	Glane_15092017_new
Processed	2017-11-12 14:28:00
Camera Model Name(s)	FC330_3.6_4000x3000 (RGB)
Average Ground Sampling Distance (GSD)	2.03 cm / 0.79 in
Area Covered	0.2737 km^2 / 27.3699 ha / 0.1057 sq. mi. / 67.6675 acres
Time for Initial Processing (without report)	32m:49s

Calibration Details :

Number of Calibrated Images	677 out of 683
Number of Geolocated Images	683 out of 683

Coordinate System :

Image Coordinate System	WGS84 (egm96)
Ground Control Point (GCP) Coordinate System	WGS 84 (egm96)
Output Coordinate System	WGS84 / UTM zone 32N (egm96)

Processing Options Details :

Detected Template	No Template Available
Keypoints Image Scale	Full, Image Scale: 1
Advanced: Matching Image Pairs	Aerial Grid or Corridor
Advanced: Matching Strategy	Use Geometrically Verified Matching: no
Advanced: Keypoint Extraction	Targeted Number of Keypoints: Automatic
Advanced: Calibration	Calibration Method: Standard Internal Parameters Optimization: All External Parameters Optimization: All Rematch: Auto, no

Figure 2. 7. Initial Processing General Summary

From Figure 2.7, provides some data about the initial processing that was done and provides a general summary of the project. The GSD of 2.03cm indicated DSM spatial resolution resulted and designated the expected DEM's accuracy. Every image was successfully geolocated (683 out of 683 images), indicated all the images were taken into account to generate the orthophoto. However, a number of calibrated images were 677 out of 683, remains 6 uncalibrated images has impacted the point cloud representation of the area surfaces above. From processing options details, it was declared that full image scale was used for keypoints extraction, which indicated a precise result although it took a longer time of extraction. The internal and external parameters of the camera were all reported optimized in the calibration process. Stated in Figure 2.7 above that DSM and the orthophoto were established in WGS 84 coordinate system. This coordinate system was further used to all the spatial products generated from this research.

The overview of initial processing indicated the next process to determine the point cloud density. The quality assessment on initial processing was emphasised to number of calibrated-uncalibrated images and the image georeferencing result. The calibrated image set and GCP error less than two times the average GSD for georeferencing designated reliable point cloud quality. To obtain the standards of the expected quality points, customisation of the parameters was required to be applied. Adjustment on numbers and distribution of the tie points and GCPs strongly affected the georeferencing result. This is why the analysis of this aspect needs to be done correctly multiple time before applying the point cloud densification and generating the DSM.

After the initial processing was done, the densification of point clouds was applied. Assesment on point cloud densification result was also based on the quality report identification. The report of increasing point cloud density has informed the details as illustrated in Figure 2.8 below.

Point Cloud Densification Details :

Image Scale	multiscale, 1/2 (Half image size, Default)
Point Density	Optimal
Mnimum Number of Matches	3
3D Textured Mesh Generation	no
LOD	Generated: no
Advanced: Image Groups	group1
Advanced: Use Processing Area	yes
Advanced: Use Annotations	yes
Time for Point Cloud Densification	02h:54m:20s
Time for Point Cloud Classification	48m:07s

Point Cloud Result Details:

Number of Processed Clusters	6
Number of Generated Tiles	2
Number of 3D Densified Points	43893599
Average Density (per m^3)	234.36

Figure 2. 8. Summary of Point Cloud Densification

From Figure 2.8 above, it is known that point cloud densification specified the 1/2 (half image size) used to speed up the processing, which has done for large projects with high overlap. This half image size allowed to state how wide the area in the image that has the key points to be extracted in comparison to the initial size of the images. The minimum numbers of matched images that used for key points matching were three images, including the minimum requirements of image number to be able to support the high-density point cloud generation. As the densification applied, the result of point cloud density is 43,893,599 with average 234, 36 points per 1 m^3.

2.1.4. Terrestrial Measurement for UAV's DEM Validation Purpose

As addressed, that the terrestrial measurement in this research was conducted for two purposes that are: (1) to collect the reference points for UAV image set georeference and (2) to provide the reference data that is needed to validate the DEM's retrieved from UAV Images. Collecting the reference points for images georeferencing has been addressed in image acquisition steps. This particular step was deliberated on terrestrial measurement for UAV's DEM validation purpose.

It is noted that terrestrial measurement technique which was used for the reference points collection was the Real Time Kinematic (RTK) differential GPS method. RTK-GPS is a satellite-based positioning system where the precise coordinates of points measured on the field are based on the differential position of the same points to the navigation satellites at a real time. The satellites conjunction with GNSS (Global

Navigation Satellites System) are GPS, GLONASS, Galileo, BeiDou, GAGAN). Real Time Kinematic (RTK)-GPS method for collecting the reference data was done by terrestrial survey at the same captured area by UAV with as shown in Figure 2.9. below:

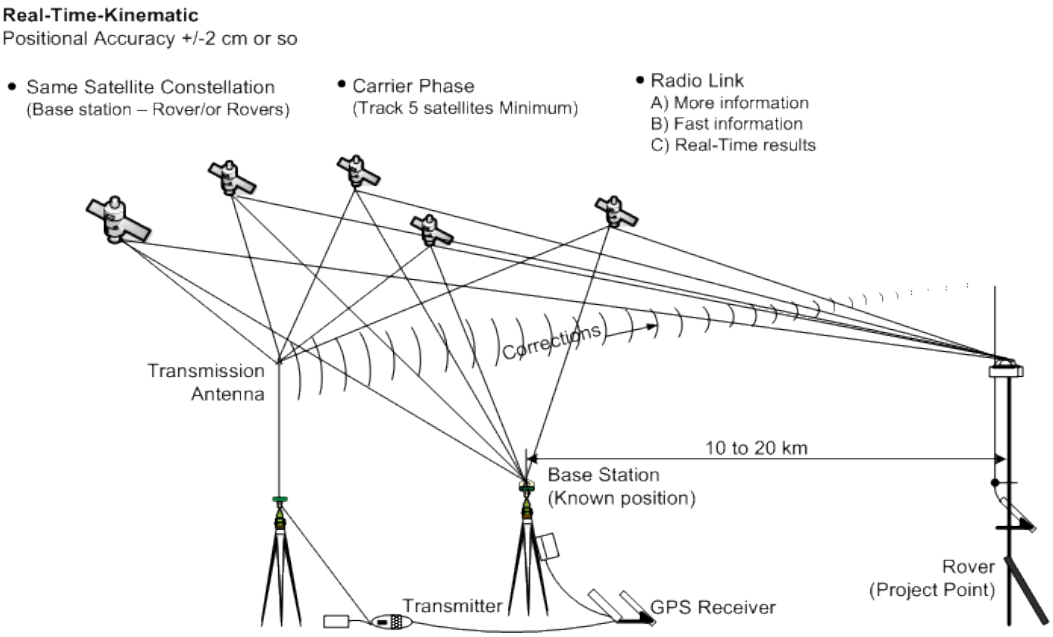

Figure 2. 9. RTK-GPS Measurement Concept. Source: (Van Sickle, 2001)

Based on the RTK-GPS concept shown in Figure 2.9 above, the terrestrial measurement was applied by moving the project point as known as rover and placed at the reference points on the field. On every position where the rover placed, the constellation of the transmission antenna and the base station have been initiated with the numbers of navigation satellites for addressing the position of the rover at the real time. In this method, there was 0,5 ppm (part per million) additional errors from the rover instrument occurred due to distances of the rover from the base station. These distances were consequenced in the 20mm XYZ accuracy of the GNSS antenna rover in every control points measured. As informed in the image acquisition process, the instrument that was used for this UAV's DEM validation purpose was also the Leica CS15 Field Controller and GS14 GNSS GPS Bluetooth Smart Antenna, as shown in Figure 2.10 below.

i). GS14 GNSS Bluetooth Antenna *ii). Smartworx Viva Interface and GPS Controller* *iii) Measurement on the field*

Figure 2. 10. RTK GPS Instrument, Smartworx Viva Interface, and Field Measurement

RTK-GPS method for UAV's DEM validation was done by measuring the coordinates and elevation of the various points on river banks and the floodplains. As the reference, points were taken from different land

cover and terrain type around the river banks for defining reliable UAV's DEM. The measurement steps of RTK-GPS method were:

1. Data Preparation and Survey Planning: preparation of map and information of the location, instrument preparation, get familiar with the tools and software used, and set up the survey strategy.
2. Field Measurement: Stated the points in the field, measured the coordinates and elevations, and store the data (measured on 29 November 2018)
3. Post Processing: download the data from GPS controller and plotting the points for the validation.

In Figure 2.11 below describes the numbers and distribution of reference points measured with RTK-GPS method.

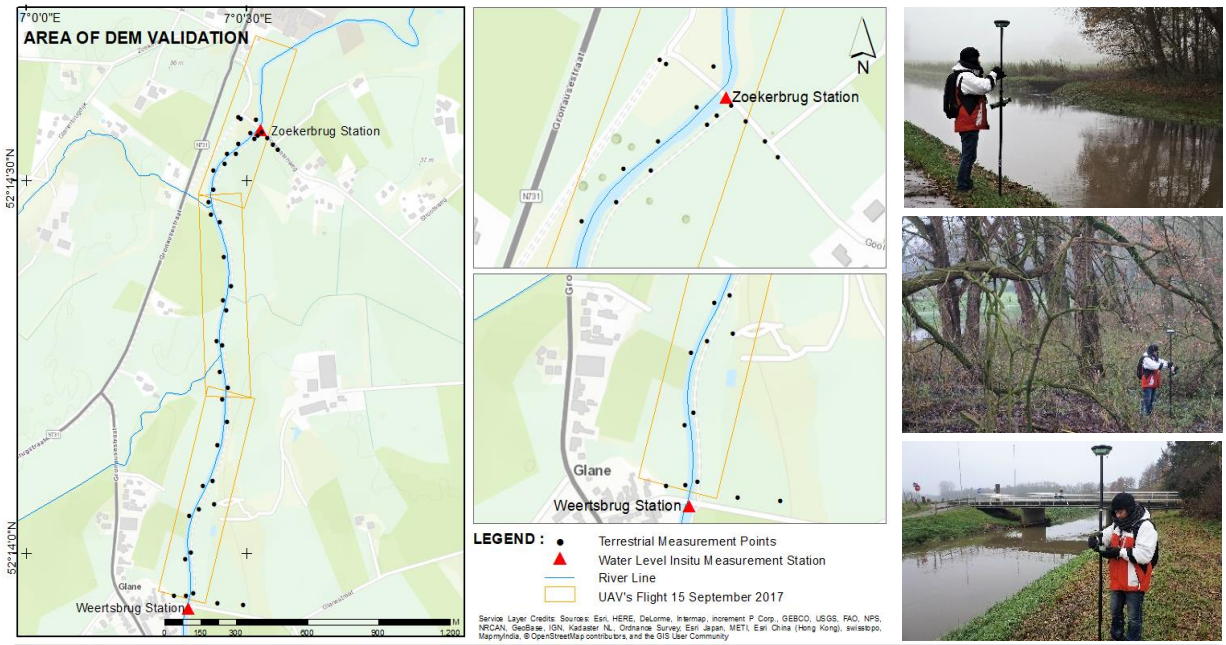

The map showing the coordinates of the reference points that were measured on 29 September 2017. The reference points measured on left and right river banks. The RTK-GPS measurement were documented in fieldwork photos on the right side.

Figure 2. 11. Distribution of The Reference Points and The Measurement Process

2.1.5. Conversion of UAV's Digital Surface Model (DSM) to Digital Elevation Model (DEM)

Multiple time densification in image processing resulted a high-density point cloud. Dense point cloud produced an accurate DSM that further determine DEM retrieved accuracy. DSM retrieved was saved as the LAS file or LAZ (zip/compressed file), a standard file format for delivery LIDAR point cloud data. LAS file was developed by *American Society for Photogrammetry and Remote Sensing* (ASPRS) to store LIDAR data retrieved by optical remote sensors (American Society for Photogrammetry and Remote Sensing, 2011). Although developing principally for LIDAR data, this format supports the exchange of any 3-dimensional X,Y,Z tuplet, include the dense matching photogrammetry data from UAV. As the research purpose stated, the DSM that represent the surfaces required to be transformed to the real terrain (DTM).

The DSM's LAS file generated from digital photogrammetry process was classified into a few different classes of land cover. The LAS file was investigated based on correctness of the land covers presented in DSM's LAS file. The classes in LAS file were differentiated based on the object's elevation such as low-medium-high vegetation, water, building, road surface, rail, tower, bridge deck, noise and ground. As the real terrain retrieval was the objective of the conversion, the ground value from different land cover was

extracted out. This means that ground extraction from different land cover has been done with involvement of the modification of the different parameter value. The ground class from UAV's DSM LAS file was later merged with a ground class that extracted out from other classes, to have a real terrain of the area as defined as DEM. In the process of extraction of ground value from other classes, the parameters were adjusted in multiple times until the reasonable ground value regained.

The transformation of the non-ground become ground class was applied in the process of using the *LAStools* software. The steps of the DSM to DEM conversion processes are presented in Figure 2.12 below:

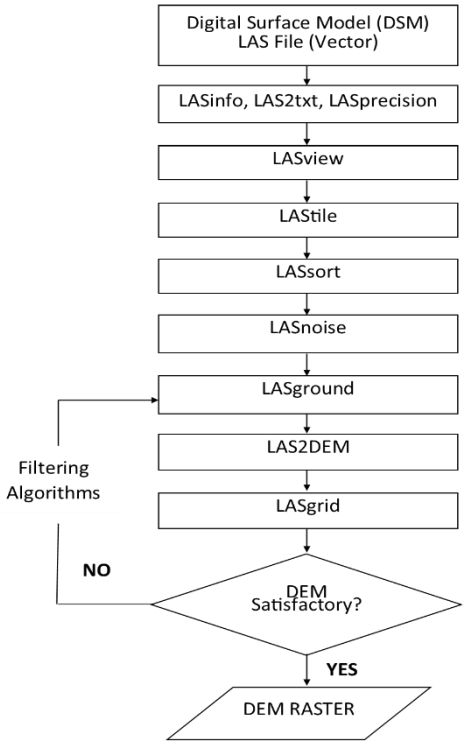

Figure 2. 12. DSM to DEM Conversion Steps

Based on the process that illustrated in Figure 2.12 above, the steps that were used for converting the DSM to DEM produced a result on every step.

1. ***LASinfo, LAStxt, and LASprecision.***
   LAS info was used to report the content of the header and warned of the user if there were difference between the header information and the point content. *Las2txt* was used to convert the *LAZ* file into a text file, also used for inspection of raw data of *LAS* file before processed. *LASprecision* was used to read the LAS format files and calculate statistics that informs whether the precision "advertised" in the header is actually in the data.

2. ***LASview.***
   It was used for quality checking of the LAS file in a full scale of the area and showed in detailed views of a cross-section or smaller area of interest. *LASview* was used for editing or deleting points as well as computing/displaying a computed TIN from (a selection of) the points. DSM retrieved was inspected for the unexpected noises that generally occurred at the dense-matching point clouds that was generated from digital photogrammetry process (Isenburg & Lavy, 2017). The inspection of DSM *LAS* file is illustrated in the Figure 2.13 below.

Low noises under the ground class occurred, will count as a ground if were not terminated. The Noises detected with profile inspections on cross sections and manually deleted.

Figure 2. 13. Noise Inspection at DSM LAS file

As seen in Figure 2.13 above, the DSM showed unexpected noise that appeared under the ground which could be included as a ground if were not terminated. This is the reason why this "lower" noise should be cut out before the conversion to the terrain. However, this DSM came out with extremely large numbers of points in one *LAS* file which was a problem to be edited due to over 5 million of point clouds. The 5 million points tolerance of processing in this function have carried out consequence in re-tiled the *LAS* file into the smaller tile with less numbers of cloud points.

After re-tiled, noises editing/deleting were re-applied to terminate the noises that could not be processed before re-tiled. It is noted that new 16 subtiles were edited in parallel and the changes that applied were saved in each subtile, included after the deleted noises. Figure 2.14 below illustrated the comparison of the re-tiled *LAS file* at before and after noise removal.

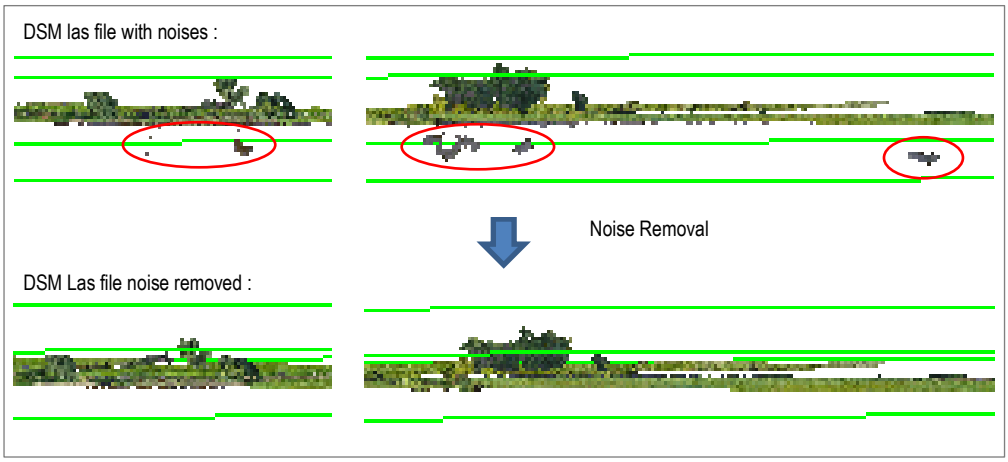

This figure demonstrated how the noises had been removed from the LAS file. After the noises removed, sub-tiles of the LAS files were processed for the conversion to the terrain model.

Figure 2. 14. Comparison before and after noise removed

3. *LAStiles.*

Tiled a potentially very large amount of LAS points from one or many files into square non-overlapping tiles of a specified size. The *"Glane_15092017"* DSM *LAS* file has 43,054,615 RGB coloured points sized 1,2 gb LAS which was oversized to process, therefore, the system gave a warning, indicating that it was necessary to re-tile. The DSM *LAS* file was then re-tiled into subtiles of 300m x 300m size and 25m of buffer to avoid edge artifacts along the boundaries. The tiling was done as illustrated in the Figure 2.15 below.

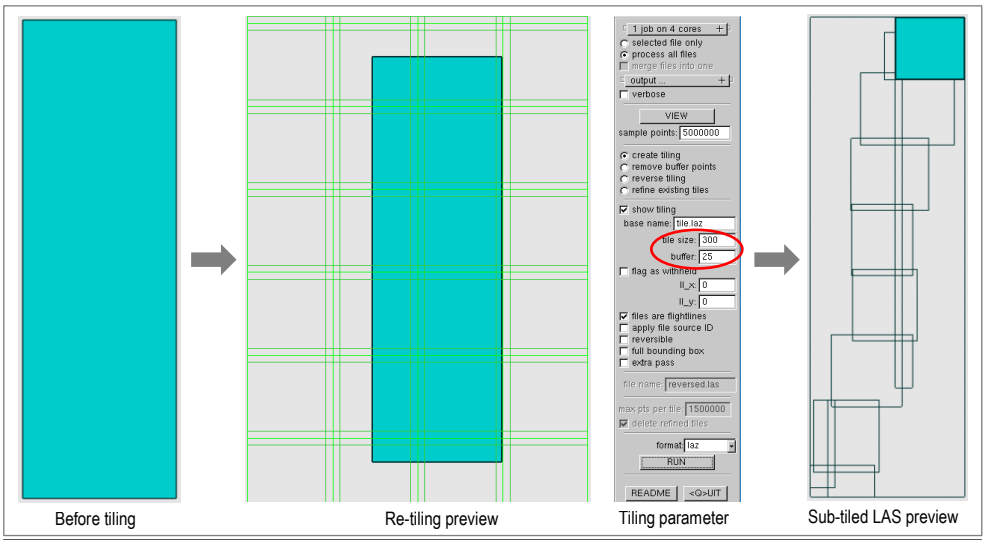

Re-tiling UAV's DSM LAS file into 16 smaller subtiles with size parameter 300mx300m (red circle). New subtiles given 25 m buffer to avoid edge artifacts. New subtiles positons previewed as in the figure.

Figure 2. 15. Re-tiling Process

Figure 2.15 above shows DSM *LAS* file was tiled into 16 new smaller sizes of subtiles and were later re-inspected in each for noise detection in *lasview* processing. The noise editing was then generated noise-cleaned subtiles which were processed in parallel on each step of DEM generating process.

4. *LASsort.*

Sorted the points of the LAS file into Z-order arranged cells of a square quad tree. For sorting *LAS* files, a bucket size was specified to determine the resolution of finest quad tree cell. *LAS* files that were part of re-tiled were benefit to specify the resolution via the number of levels of subtiling. This has the advantage that both the tiled and the subtiled could be used during streaming processing. In sorting parameters, the default size of bucket and level were intended to used instead re-sizing the bucket, due to the fact that new bucket size will either destroy re-tiling result or reorder the points without the benefit of new subtiles finalization. Re-ordering the tiles was done with command: ***lassort –lof file_list.3080.txt –cores 4 –odir "c:\Hariady_Thesis\LAS_files\01_laasort" –odix "_s" –olaz*** as shown in Figure 2.16 below

```
lassort -lof file_list.3080.txt -cores 4 -odir "c:\Hariady_Thesis\LAS_files\01_lassort" -odix "_s" -olaz
done with 'c:\Hariady_Thesis\LAS_files\01_lassort\glane_363600_5788800_s.laz'. took 1.163 sec.
done with 'c:\Hariady_Thesis\LAS_files\01_lassort\glane_363600_5788600_1_s.laz'. took 3.625 sec.
done with 'c:\Hariady_Thesis\LAS_files\01_lassort\glane_363800_5788600_1_s.laz'. took 6.354 sec.
done with 'c:\Hariady_Thesis\LAS_files\01_lassort\glane_363800_5789400_s.laz'. took 4.13 sec.
done with 'c:\Hariady_Thesis\LAS_files\01_lassort\glane_363800_5789000_1_s.laz'. took 15.006 sec.
done with 'c:\Hariady_Thesis\LAS_files\01_lassort\glane_363800_5789600_1_s.laz'. took 5.309 sec.
done with 'c:\Hariady_Thesis\LAS_files\01_lassort\glane_363800_5790000_s.laz'. took 2.582 sec.
done with 'c:\Hariady_Thesis\LAS_files\01_lassort\glane_363800_5788800_s.laz'. took 21.587 sec.
done with 'c:\Hariady_Thesis\LAS_files\01_lassort\glane_364000_5789000_s.laz'. took 3.269 sec.
done with 'c:\Hariady_Thesis\LAS_files\01_lassort\glane_363800_5789200_1_s.laz'. took 21.337 sec.
done with 'c:\Hariady_Thesis\LAS_files\01_lassort\glane_363800_5789800_1_s.laz'. took 8.392 sec.
done with 'c:\Hariady_Thesis\LAS_files\01_lassort\glane_364000_5789200_s.laz'. took 5.972 sec.
done with 'c:\Hariady_Thesis\LAS_files\01_lassort\glane_364000_5789400_s.laz'. took 7.979 sec.
done with 'c:\Hariady_Thesis\LAS_files\01_lassort\glane_364000_5789600_s.laz'. took 8.093 sec.
done with 'c:\Hariady_Thesis\LAS_files\01_lassort\glane_364000_5789800_s.laz'. took 13.153 sec.
done with 'c:\Hariady_Thesis\LAS_files\01_lassort\glane_364000_5790000_1_s.laz'. took 11.933 sec.
```

*The sorting algorithm (red square highlighted) above means that **lassort** was applied to 16 subtiles in **list of file (lof) file_list.3080.txt** using **4 cores** (maximum numbers) of CPU, and the sorting result files were stored in **c:\Hariady_Thesis\LAS_files\01_laasort** given appendix **"s"** for each 16 output **laz** files.*

Figure 2. 16. Report of LAS file sorting

Seen from Figure 2.16 above the processing time for sorting 16 subtiles reported, indicated all the subtiles were sorted successfully.

5. *LASnoise*

Isolated or reclassified the noise to a certain class so later would not lead the DEM conversion to the incorrect terrain result. After the points of each tile were sorted, it was found out that points of clouds below the ground were not the only noises problem, the fact that many unclassified points which considered as noises were also scattered in the *LAS file*. It is noted that the conversion process itself was done in numbers of trials and the results were always indicated this noises problem. This noise problem was handled correctly using this *lasnoise* function, with flagged certain numbers of noises in certain grid sizes or distances (x,y,z). The noises flagged were applied to all 16 subtiles with the command: ***lasnoise -i lof file_list.11600.txt –cores 4 –step_xy 2 –step_z 1 – isolated 15 –odir "c;\Hariady_Thesis\LAS_files\02_lasnoise_new "-odix "_n" –olaz.*** It means that list of 16 subtiles *file_list.11600.txt* were processed using *4 CPU's cores* with grid size *(XY) 2 x 2m* and height *(Z) 1 meter*, *isolated 15 points*, stored in *"c;\Hariady_Thesis\LAS_files\02_lasnoise_new "* and given *appendix files "_n"* with *laz* format file. Below is the Figure 2.17 shows the initiated noises and the effect on the DEM resulted that were addressed in this research.

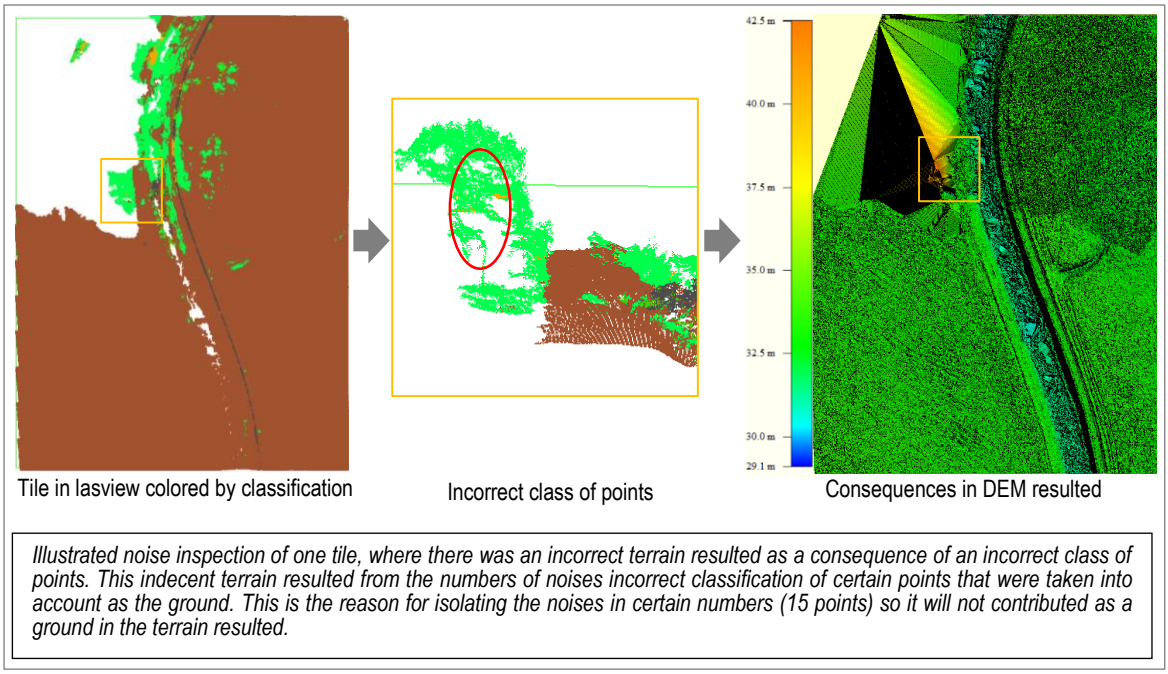

Illustrated noise inspection of one tile, where there was an incorrect terrain resulted as a consequence of an incorrect class of points. This indecent terrain resulted from the numbers of noises incorrect classification of certain points that were taken into account as the ground. This is the reason for isolating the noises in certain numbers (15 points) so it will not contributed as a ground in the terrain resulted.

Figure 2. 17. Sub-tile Noise Inspection

Figure 2.17 above demonstrates incorrect terrain elevation range due to an extreme elevation of one very small area on the left bank that reaches above 40 m height which did not exist in the area, based on the field observation. However, this noise problem was later solved by numbers of customizations on *lasnoise* parameters combined with the noise removal/reclassification manually on each tile of *LAS files*. This noise inspection was also functioned as the reclassification of points from other classes to ground class if only the points should have counted as a ground.

6. *LASground*

This is the most important step of the DTM generation, crucial for bare-earth extraction. In this step, the tool classified LAS points into ground points (class = 2) and non-ground points (class = 1). *Lasground* worked very well in natural environments such as mountains, forests, fields, hills, or another

terrain with few man-made objects. This terrain determination applied with ground class *(class 2)* extraction from the DSM las file and only *class 2 (ground)* points were taken into account as the terrain.

Extraction to the ground class was applied in two different ways; (1) extra fine nature (default) algorithm and (2) algorithm of modification on ground filtering parameter. For (1) extra fine nature algorithm, the command applied was ***lasground –lof file_list.14332.txt –cores 4 –no_bulge –nature –extra_fine –odir "c:\Hariady_Thesis\LAS_file\02_lasground_extra" –odix "_g" –olaz***. The command means that list of *16 subtiles* in the *list of file (lof) list 14332.txt* were processed with *4 cores* of computer's CPU without *bulge* expected using a *nature* area condition on *extra fine* quality and the result stored in *"c:\Hariady_Thesis\LAS_file\02_lasground_extra"* given *appendix "g"on every file resulted* in *laz* format file. The processing report of ground class extraction with "extra fine nature" was presented as in Figure 2.18 below.

```
done with 'c:\Hariady_Thesis\LAS_files\without_lasnoise\02_lasground\glane_363600_5788600_1_1_s_g.laz'. total time 6.477 sec.
done with 'c:\Hariady_Thesis\LAS_files\without_lasnoise\02_lasground\glane_363600_5788800_s_g.laz'. total time 12.167 sec.
done with 'c:\Hariady_Thesis\LAS_files\without_lasnoise\02_lasground\glane_363800_5788600_1_s_g.laz'. total time 24.753 sec.
done with 'c:\Hariady_Thesis\LAS_files\without_lasnoise\02_lasground\glane_363800_5788800_1_s_g.laz'. total time 52.398 sec.
done with 'c:\Hariady_Thesis\LAS_files\without_lasnoise\02_lasground\glane_363800_5789000_1_s_g.laz'. total time 48.094 sec.
done with 'c:\Hariady_Thesis\LAS_files\without_lasnoise\02_lasground\glane_363800_5789200_1_1_s_g.laz'. total time 54.35 sec.
done with 'c:\Hariady_Thesis\LAS_files\without_lasnoise\02_lasground\glane_363800_5790000_s_g.laz'. total time 4.454 sec.
done with 'c:\Hariady_Thesis\LAS_files\without_lasnoise\02_lasground\glane_363800_5789400_1_s_g.laz'. total time 47.963 sec.
done with 'c:\Hariady_Thesis\LAS_files\without_lasnoise\02_lasground\glane_364000_5789000_s_g.laz'. total time 7.269 sec.
done with 'c:\Hariady_Thesis\LAS_files\without_lasnoise\02_lasground\glane_363800_5789800_1_s_g.laz'. total time 25.129 sec.
done with 'c:\Hariady_Thesis\LAS_files\without_lasnoise\02_lasground\glane_364000_5789400_s_g.laz'. total time 14.899 sec.
done with 'c:\Hariady_Thesis\LAS_files\without_lasnoise\02_lasground\glane_364000_5789200_s_g.laz'. total time 21.487 sec.
done with 'c:\Hariady_Thesis\LAS_files\without_lasnoise\02_lasground\glane_364000_5789600_s_g.laz'. total time 21.432 sec.
done with 'c:\Hariady_Thesis\LAS_files\without_lasnoise\02_lasground\glane_363800_5789600_1_1_1_s_g.laz'. total time 54.235 sec.
done with 'c:\Hariady_Thesis\LAS_files\without_lasnoise\02_lasground\glane_364000_5789800_s_g.laz'. total time 28.647 sec.
done with 'c:\Hariady_Thesis\LAS_files\without_lasnoise\02_lasground\glane_364000_5790000_1_1_1_s_g.laz'. total time 28.866 sec.
```

The processing report showing the processing time of ground extraction on 16 subtiles. Shown on each result file the appendix were given on every processing applied; sorting (_s) and ground (_g), and the .laz output format file.

Figure 2. 18. Report of Ground Class Extraction with ***Extra Fine Nature***

Ground extraction was also applied to modification of the ground filtering parameters; *Offset, Spike* and *standard deviation. Offset* defined the level of which the points above the estimated ground that included in the terrain model. *Spike* described the distance above the coarsest *TIN* for which the points are being accepted as terrain. *Standard deviation* removed objects lying close to the terrain that were not necessarily part of the terrain. This filtering parameter modification on ground class were produced with command: ***lasground –lof file_list.10220.txt –cores 4 –bulge 0 –offset 0.02 -spike 0.3 –stddev 2 –odir c:\Hariady_Thesis\LAS_file\02_lasground_withparameter" –odix "gp" –olaz".*** The command means that list of *16 subtiles* in the *list of file (lof) list 10220.txt* were processed with *4 cores* of CPU with *no bulge* expected using *0.02 m* of *offset*, *0.3 m* of *spike*, and *2 m* of *standard deviation.* The result stored in *"c:\Hariady_Thesis\LAS_file\02_lasground_withparameter"* given *appendix "gp"*on every result in *laz* format file. Ground class extraction with these filtering parameters customization was reported as seen in Figure 2.19 below.

```
done with 'c:\Hariady_Thesis\LAS_files\without_lasnoise\02_lasground_withparameter\glane_363600_5788600_1_1_sgp.laz'. total time 4.921 sec.
done with 'c:\Hariady_Thesis\LAS_files\without_lasnoise\02_lasground_withparameter\glane_363600_5788800_sgp.laz'. total time 9.996 sec.
done with 'c:\Hariady_Thesis\LAS_files\without_lasnoise\02_lasground_withparameter\glane_363800_5788600_1_sgp.laz'. total time 18.922 sec.
done with 'c:\Hariady_Thesis\LAS_files\without_lasnoise\02_lasground_withparameter\glane_363800_5788800_1_sgp.laz'. total time 50.453 sec.
done with 'c:\Hariady_Thesis\LAS_files\without_lasnoise\02_lasground_withparameter\glane_363800_5789000_1_sgp.laz'. total time 46.64 sec.
done with 'c:\Hariady_Thesis\LAS_files\without_lasnoise\02_lasground_withparameter\glane_363800_5789200_1_1_sgp.laz'. total time 48.418 sec.
done with 'c:\Hariady_Thesis\LAS_files\without_lasnoise\02_lasground_withparameter\glane_363800_5790000_sgp.laz'. total time 3.965 sec.
done with 'c:\Hariady_Thesis\LAS_files\without_lasnoise\02_lasground_withparameter\glane_363800_5789400_1_sgp.laz'. total time 47.963 sec.
done with 'c:\Hariady_Thesis\LAS_files\without_lasnoise\02_lasground_withparameter\glane_364000_5789000_sgp.laz'. total time 7.165 sec.
done with 'c:\Hariady_Thesis\LAS_files\without_lasnoise\02_lasground_withparameter\glane_363800_5789800_1_sgp.laz'. total time 21.684 sec.
done with 'c:\Hariady_Thesis\LAS_files\without_lasnoise\02_lasground_withparameter\glane_364000_5789400_sgp.laz'. total time 14.795 sec.
done with 'c:\Hariady_Thesis\LAS_files\without_lasnoise\02_lasground_withparameter\glane_364000_5789200_sgp.laz'. total time 20.286 sec.
done with 'c:\Hariady_Thesis\LAS_files\without_lasnoise\02_lasground_withparameter\glane_364000_5789600_sgp.laz'. total time 21.483 sec.
done with 'c:\Hariady_Thesis\LAS_files\without_lasnoise\02_lasground_withparameter\glane_363800_5789600_1_1_1_sgp.laz'. total time 49.223 sec.
done with 'c:\Hariady_Thesis\LAS_files\without_lasnoise\02_lasground_withparameter\glane_364000_5789800_sgp.laz'. total time 30.629 sec.
done with 'c:\Hariady_Thesis\LAS_files\without_lasnoise\02_lasground_withparameter\glane_364000_5790000_1_1_1_sgp.laz'. total time 29.553 sec.
```

Seen the processing of ground extraction were applied on 16 subtiles in a certain time. Each result file given the appendix from every processing applied; sorting (_s) and ground with parameter (gp), and the .laz format file for

Figure 2. 19. Report of Ground Class Extraction with ***Filtering Parameter Modification***

7. LAS2dem

This process read the *LAS* format, triangulated them temporarily into a *TIN*, and then rastered the *TIN* onto a DEM. The tool also can generated the *'-elevation'*, the *'-slope'*, the *'-intensity'*, the *'-RGB'* values, or a *'-hillside'* or *'-grey'* or *'-false'* colouring. The output is either in *BIL, ASC, IMG, FLT, XYZ, DTM, TIF, PNG or JPG* format.

Two sets of generated ground class that were later converted into a DEM resulted in two sets of terrain platforms. Ground class with *extra fine nature* filtered were converted to DEM with command: ***las2dem –lof file_list 9496.txt –keep_class 2 –use_tile_bb –odir "c:\Hariady_Thesis\LAS_files\03_las2dem_extra" –odix "_dtm" –obil –step 0.02 –cores 4***, which means that list of 16 subtiles in *file_list 9496.txt* were processed with only ground class *(class 2)* were *kept* and *bounding box (bb)* of each tile was used as the boundary. The results were saved in the folder "*c:\Hariady_Thesis\LAS_files\03_las2dem_extra"* with *appendix* "*_dtm"* and each DEM subtiles generated in *0.02 m grid size (step)* accuracy. The process was utilised *4 cores* (maximum number) of computer's CPU in parallel, and the output files were in *bil* format file. Results on *converted to DEM* process were reported as shown in Figure 2.20 below.

```
WARNING: there were 1 duplicate rasters
there were 319884 clipped rasters (and 0 unclipped ones)
there were 161373 clipped rasters (and 0 unclipped ones)
WARNING: there were 1 duplicate rasters
there were 154636 clipped rasters (and 0 unclipped ones)
WARNING: there were 1 duplicate rasters
there were 266307 clipped rasters (and 0 unclipped ones)
there were 358515 clipped rasters (and 0 unclipped ones)
there were 183979 clipped rasters (and 0 unclipped ones)
there were 249127 clipped rasters (and 0 unclipped ones)
there were 155632 clipped rasters (and 0 unclipped ones)
there were 21312 clipped rasters (and 0 unclipped ones)
there were 1444388 clipped rasters (and 0 unclipped ones)
there were 406107 clipped rasters (and 0 unclipped ones)
there were 296226 clipped rasters (and 0 unclipped ones)
there were 142139 clipped rasters (and 0 unclipped ones)
there were 44251 clipped rasters (and 0 unclipped ones)
there were 1429840 clipped rasters (and 0 unclipped ones)
there were 335961 clipped rasters (and 0 unclipped ones)
```

Illustrated numbers of ground class points that were clipped as a raster from each of 16 subtiles.

Figure 2. 20. Report of Conversion to DEM ***to Extra Fine Nature Ground***

Conversion to a DEM also applied to the ground class that were created with *ground filtering customized parameter*, with the command: **l*as2dem –lof file_list 10156.txt –keep_class 2 –use_tile_bb –odir "c:\Hariady_Thesis\LAS_files\03_las2dem_withparameter" –odix "_dtmp" –obil –step 0.02 –cores 4***. The command means that list of 16 subtiles in *file_list 10156.txt* were processed with only kept the ground class *(class 2)* and each tile's *bounding box (bb)* were used as the boundary. The results were saved in the folder "*c:\Hariady_Thesis\LAS_files\03_las2dem_withparameter"* with *appendix* "*_dtmp"* and each DEM subtiles produced in *0.02 m grid size (step)* accuracy. The process was applied with maximizing *4 cores* of computer's CPU in parallel, and the output was in *bil* format file. Conversion to DEM on this modified parameter setup was also reported as seen in Figure 2.21 below.

```
WARNING: there were 1 duplicate rasters
there were 315319 clipped rasters (and 0 unclipped ones)
there were 288988 clipped rasters (and 0 unclipped ones)
there were 172619 clipped rasters (and 0 unclipped ones)
there were 421871 clipped rasters (and 0 unclipped ones)
there were 319152 clipped rasters (and 0 unclipped ones)
there were 405953 clipped rasters (and 0 unclipped ones)
there were 413944 clipped rasters (and 0 unclipped ones)
there were 203428 clipped rasters (and 0 unclipped ones)
there were 1464793 clipped rasters (and 0 unclipped ones)
there were 64264 clipped rasters (and 0 unclipped ones)
there were 457389 clipped rasters (and 0 unclipped ones)
there were 243798 clipped rasters (and 0 unclipped ones)
there were 339210 clipped rasters (and 0 unclipped ones)
there were 97507 clipped rasters (and 0 unclipped ones)
there were 405099 clipped rasters (and 0 unclipped ones)
there were 1836656 clipped rasters (and 0 unclipped ones)
```

Seen the numbers of ground class points that were clipped as a raster from each of 16 subtiles.

Figure 2. 21. Report of Conversion to DEM to ***Filtering Parameters Modification Ground***

8. LASgrid

The 16 sets of DEM subtiles were later gridded onto raster file with a specific number of points in one subtile. The gridded process was done by using *lasgrid* function with the most important parameter used is *"-step n"*, which used to specify the *n x n* area of the *LAS points* that have been gridded.

Similar to the previous functions, this step was also applied in two different sets of DEMs. DEM sets subtiles with *extra fine nature* ground were gridded with command: ***lasgrid –lof file_list 10168.txt –merged –step 0.02 –odir "c:\Hariady_Thesis\LAS_files\04_lasgrid_extra" –o "merged_2cm_nooptionx.bil",*** which means that list of 16 subtiles in the list of file (lof) *file_list 10168.txt* were processed to generate *2cm* of *n x n* in one grid of the *las points,* and all the subtiles *merged* into one new result file in *bil* file format. The new grid file was stored in *"c:\Hariady_Thesis\LAS_files\04_lasgrid_extra"* with output file name is *"merged_2cm_nooptionx.bil"*. Gridded was applied as well to the modified ground filter parameters, with the command : ***lasgrid –lof file_list 7646.txt –merged –step 0.02 –odir "c:\Hariady_Thesis\LAS_files\04_lasgrid_withparameter" –o "merged2cm_parameter.bil".*** The command means that 16 subtiles in *file_list 7646.txt* were merged into one new grid file with 2cm of grid resolution, stored in *c:\Hariady_Thesis\LAS_files\04_lasgrid_withparameter* with the output file name *"merged2cm_parameter.bil"* in *bil* format file.

This gridded process resulted in two sets of terrain models based on the ground filtering used; the *extra fine nature's* DEM and the ground filtering parameters modification's DEM. These are two main DEMs generated, besides numbers of DEMs that were generated from trials in this research. These two DEMs have the same resolution which very high; 2cm accuracy/grid resolution. Two high-resolution DEMs were later aggregated to 40cm grid resolution for each ground filtered, resulting in four elevation models that were later validated with reference points from the terrestrial measurement.

2.2. Examine the accuracy of DEM from UAV

Theoretically, the spatial resolution of the DEM generated will be the derivative result from Ground Sampling Distance (GSD) of the UAV's image. As the GSD of this research UAV's images were about 2cm, the accuracy of resulted DEM were similar. However, the application of the DEM generated from this research was for hydraulics modelling purposes, affected the level of DEM's accuracy that were used. Therefore the aggregation of DEM grid resolution to 40cm grid size were applied. The DEMs with two different grid resolution were examined by comparing the Z coordinates of the reference points from the terrestrial measurement and measured at UAV's DEMs.

2.2.1. Generate high accuracy DEM

Due to critical impact of the DEM raster grid size for hydraulics modelling uses, the level of expected accuracy needed to be inspected precisely. To generate the reasonable grid size of DEM, a number of parameters were adjusted. As noted, the most important parameter *'-step n'* specified the *n x n* area of points that were gridded on one raster (or pixel), a number of different values were defined to this parameter. This resulted two different grid sizes. The results on different values applied on these grid sizes were compared each other for stated the best fit grid size based on the DEM application purpose.

2.2.1. Validation of UAV's DEM with DTM from Terrestrial Measurement

From the terrestrial measurement, The RTK GPS coordinates (X, Y, and Z) of reference points were obtained from the left and right banks of the river. These references were overlaid on the UAV's DEMs surfaces, and the Z coordinate (vertical) values were extracted for all DEMs. The elevations (Z coordinate) derived from the DEM output surfaces were later compared with the elevation from the terrestrial survey

at the same X,Y coordinates. The different elevation set was compared at the same cross sections (river left and right banks) from the survey. This comparison of the cross sections was effectively distinguished the profiles of the DEMs generated with the reference terrain profile. This is the validation method that was applied to UAV's DEMs generated which resulted in one set of the DEM, then were used for flood water level extent determination. The assessment on this validation method was based on the Root Mean Square Errors (RMSE) of each DEM products to the reference DTM, as shown in the formula below.

$$\mathrm{RMSE} = \sqrt{\frac{\sum_{i=1}^{n} \left(P_i - O_i\right)^2}{n}}$$

The RMSE value was given by averaging the residual squares between predicted (P) and observed (O) values, which can be positive or negative as the predicted value under or overestimates the observed value. The smallest value of RMSE from a certain set of DEM compared with DTM from terrestrial measurement utilized as the DEM for flood water level extent estimation.

2.3. Application of UAV's DEM and SAR Imagery Observation for water levels and flood extents estimation

It is noted that water availability observation from the remote sensing technique was currently the most feasible method for information extraction of the water level and flood extension (Greifeneder et al., 2014; Ouled Sghaier, Hammami, Foucher, & Lepage, 2018; Papastergios A, Chini M, & Parcharidis I, 2016; Schumann & Moller, 2015). SAR-derived observation is one of the remote sensing applications that used for inundated area detection due to flooding event. Flood information retrieved from SAR imagery required the elevation platform to be used for quantifying the water levels and the flood extents. In this research, the method of water levels and flood extents quantification from SAR Imagery and UAV's DEM was composed in three steps: (1) Pre-processing of SAR images (2) Image classification for flood extent retrieval and (3) Water levels estimation from classified image and UAV's DEM.

2.3.1. Pre-processing of SAR Images

SAR Imagery that was used in this research was the Sentinel-1 images from ESA (European Space Agency), with acquisition mode Interferometric Wide (IW), which means acquired with 250 km swath at 5 m by 20 m spatial resolution (single look). The images were pre-processed with applications that essentially applied to the SAR images which were; *terrain correction, subsetting* to the research area, and *speckle filtered*. *Terrain correction* was done by corrected the systematic errors of the sensor and topography platform-induced geometry that cause terrain distortion when the sensor was not pointed at nadir position. Correction on terrain distortion was also functioned as geo-referencing to located the image on the earth system. *Subseting* was to narrow the image to the certain area of research. *Speckle removal* was applied by removing the noises that were occurred on the images due to interference from scatters with the random phase in the SAR images to the true backscatter value.

These pre-processing steps were applied using *SNAP (Sentinel Application Platform)* software as illustrated in Figure 2.22 below.

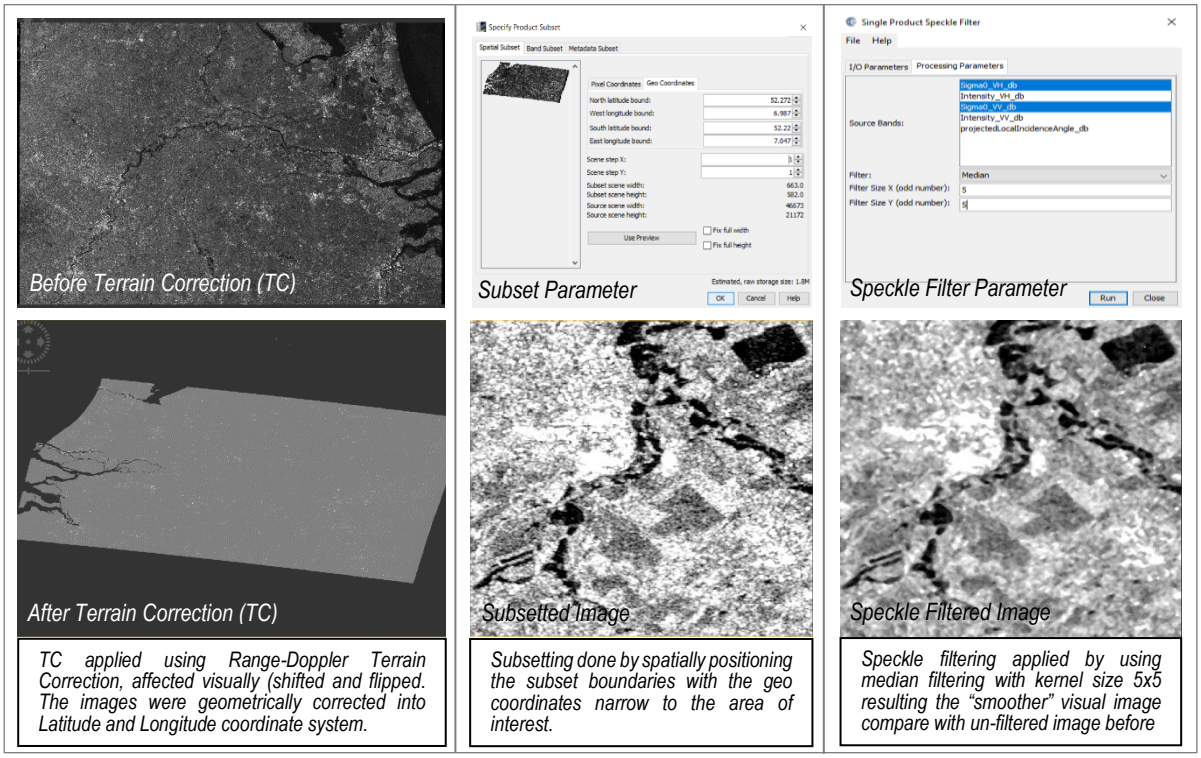

Figure 2. 22. Pre-processing: Terrain Correction, Subseting, and Filtering

2.3.2. Image Classification for Flood Extent Retrieval

Image classification was applied to produce maps consist of dry and flooded pixels from interpretations process of the image. The interpretation of SAR images was based on the sensor characteristics of *geometric spatial resolution, wavelength, incidence angle, and polarization* (Schumann & Moller, 2015). Every sensor characteristics has its own sensitivity that affects the water pixel investigation and extraction from the image. As the Sentinel-1 images utilized in this research, it has the same specification for all images which has 10 m spatial resolution and 12 days revisit time.

It is noted that the wavelengths that were used by radar sensors for flood monitoring were ranged from 30 to 4 cm and include L, C, and X Band (Čotar, Oštir, & Kokalj, 2016; Kwak & Young-joo, 2017; Manjusree, Prasanna Kumar, Mohan Bhatt, Srinivasa Rao, & Bhanumurthy, 2012). The Sentinel-1 images that were used in this research were the C Band, which have been proved very useful for flood detection in the herbaceous and wooded wetland (Brisco, Kapfer, Hirose, Tedford, & Liu, 2011). It is aware that the incidence angle was the angular deviation of incidence signal from nadir position, lower and higher the incidence angle when the sensor captured the image has its own effect on the water backscatter value in the image. The incidence angle of each image was depended on the timing when the image captured by the satellite either with ascending or descending orbit. This research has used Sentinel-1 images with incidences angles from both orbits for flood water level extraction. Utilized the images with different incidence angles with the same method based on the facts that the area located in flat terrain where topography did not much affect the side looking SAR satellite sensor. Another consideration also based on the research that was addressed the incidence angle differences were only affected on water bodies extraction of water surfaces with vegetation or rough surfaces due to wind/wave (Twele, Cao, Plank, & Martinis, 2016). Therefore, without further investigation on the influence of vegetation and surface roughness to SAR images incidence angle, this research has decided to apply the flood water level estimation using images with both angles.

Knowing that polarisation of microwave defined the direction of transmitted and reflected signals from electric field vector refers to the geometrical plane (Clement, Kilsby, & Moore, 2017). This direction is either horizontal (H) or Vertical (V) in relation to the satellite transmitter/receiver, generating four types polarisations: HH, HV, VH, and VV. Although each polarisation could be utilized for flood extraction, the differences on backscatter signal affecting the accuracy of the flood maps generated. As informed that the Sentinel-1 images in this research came with VH and VV polarisation, the observations on these two were done before select which polarisation would be used.

Visually comparison on two different bands of every image were applied to *sigma_VH* and *sigma_VV* band image. These two different bands were first converted from linear to decibel (db) to visualize a higher presence of grey pixels and reduce extreme values. Before converted to decibel, the image had an extensive value range and only very light object appeared sharp leads to difficulties on water bodies extraction. Being converted to decibel made the sigma bands *(VH and VV)* was in logarithmic scale, meaning that the values were more evenly distributed over black and white color range. After each polarisation band converted to db, then the comparison between this two polarisation was done as shown in Figure 2.23 below.

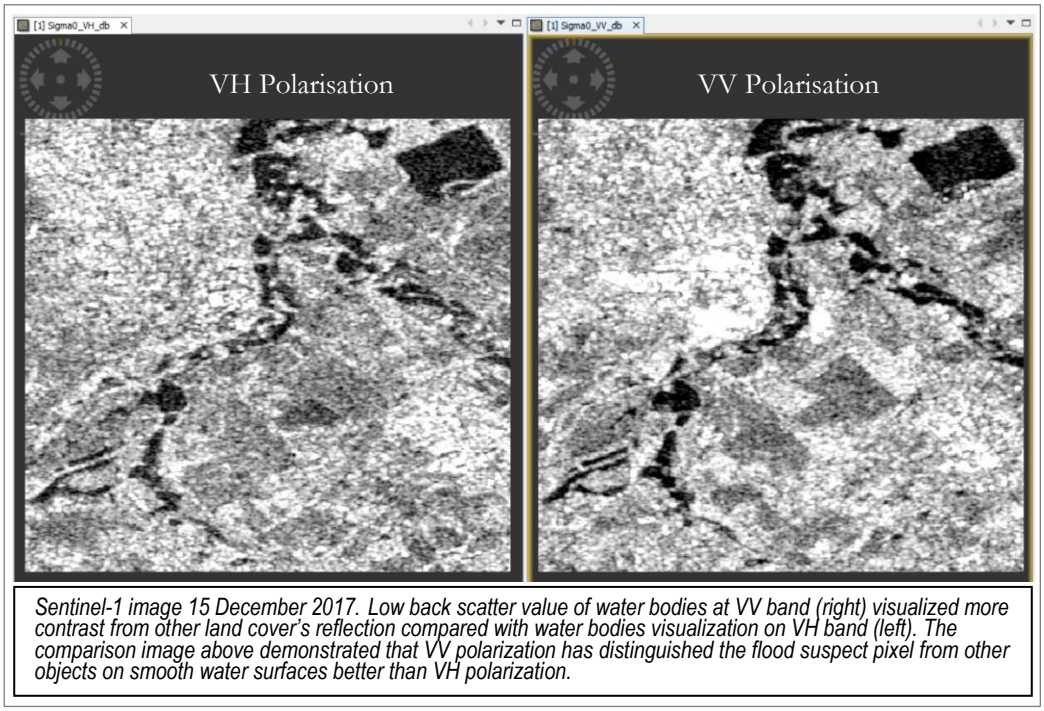

Figure 2. 23. Visual Comparation of VH and VV Polarization on Flooding Monitoring from Sentinel-1 images

Figure 2.23 above shows the Sentinel-1 image with acquisition date 15 December 2017 captured the Dinkel River including research area. The image was captured a day after the flood water level has reached the peak, refer to the actual news from Waterschap Vechtstromen at 14 December 2017 (Vechtstromen, 2017). Based on this visual inspection, VV polarization (sigma_VV_db_band) at the right slightly more enhanced to presents water body reflection compare with VH polarization (sigma_VH_db band) at the left image. Furthermore, the similar comparison was also done to few other "flooded" image, to ensure the decision on using polarization type. This observations of VV polarization on flood water detection has been a substance reason for using this polarization from every image used.

In this research, filtering algorithm application was found essentially supported to determine the backscatter value of flood water bodies. Noticed that image filtering purpose is to reduce unwanted noise and improve

the visual quality of an image, filtering also applied for smoothing the image which could corrupt the intensity, illumination, and contrast of the image (Chandel & Gupta, 2013). The comparison which underlies the use of one filtering method illustrated in Figure 2.24 below.

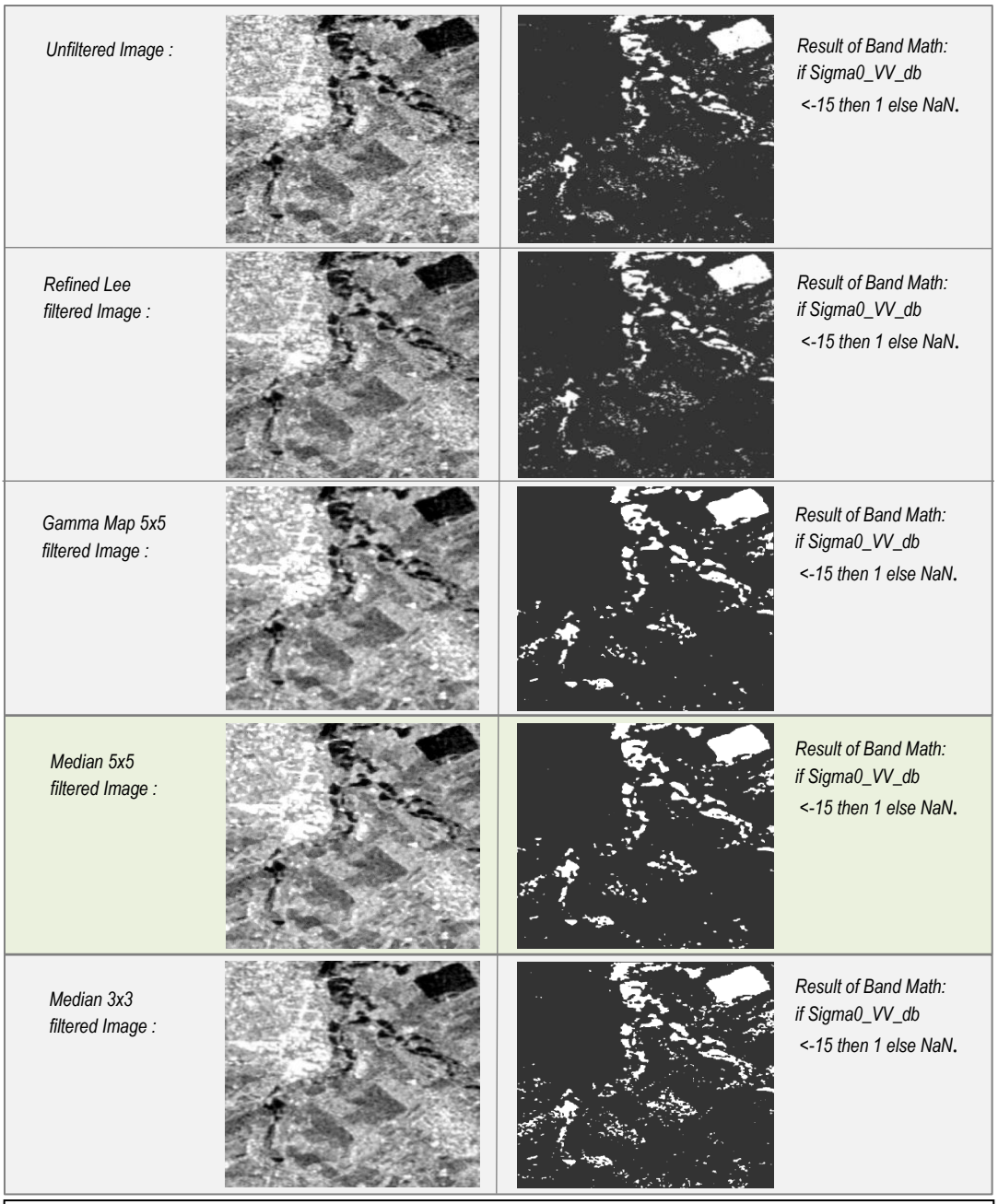

Showed the differences at before and after filtering, with each band math result of every image. Seen the sigma0_VV_db images on the left and flood treshold value applied on the right. The band math results maps illustrated the differences on water bodies extraction that derives as consequences of the image filtering.

At the unfiltered image and refined lee filtered image, noises appeared misleading water bodies backscatter values. Median filtering 3x3 image at the bottom still shown noise issue as well.

Application of gamma map and median filtering established more reasonable results. Speckle issues on the band math results of these two filter algorithm's results are very less. The size of matrix 5x5 were proven positively affected the band math result

Figure 2. 24. Comparison on Image Filtering of Sentinel-1 Images

The Figure 2.24 above addresses that median 5x5 filtering algorithm was stated to be used after multiple times of image filtering using three different algorithms; Refined Lee, Gamma Map, and Median itself. Using median algorithm does not form new unrealistic pixel values when the filter straddles an edge. Therefore this median filter still reliable at preserving sharp edges (Saxena & Rathore, 2013). Kernel matrix size 5x5 was used based on the concern of the neighbourhood pixel numbers that had affected by new replacement pixel values were less compared with using bigger kernel size such as 7x7 and 9x9. Big size kernel matrix leads to the smoother image nevertheless misplacing the backscatter value that consequent to incorrect water pixel value retrieved. The smaller kernel size 3x3 also tried to use and it still resulted incorrect the water backscatter value due to a large amount of uncertainties of flooded pixels. The comparison applied ensured *median filtering algorithm* with kernel matrix size *5x5* is used for all time series images.

2.3.3. Water Levels Retrieval from Classified Image with UAV's DEM as the platform

The water pixels that indicated permanent water bodies and flood extent area at the flooding events were occurred from image classification process, distinguished the numbers of dry and inundated images. The water level estimation was composed in two compulsory steps which were; (1) The extraction of flood extent from SAR images and (2) Water level estimation by merging the flood extent polygon with the DEM retrieved from UAV.

The first step, the flood extent extraction from SAR images was applied by stated the threshold value of backscatter value that was indicated flood. This flood backscatter value was determined by colour composite method between the most flooded image and one dry image (chosen). The created colour composite image started by creating a stack of two images; one dry image and one the most flooded image. The "dry" image selected was at acquisition date 17 September 2017, two days after image acquisition with the UAV on 15 September 2017 when the research area was not inundated, and the water flows inside the riverbanks. The image with most flooded event used is at 15 December 2017, this is when the water already over banks and inundated the floodplains area surround. Two stacked images were later overlaid in steps as shown in Figure 2.25 below.

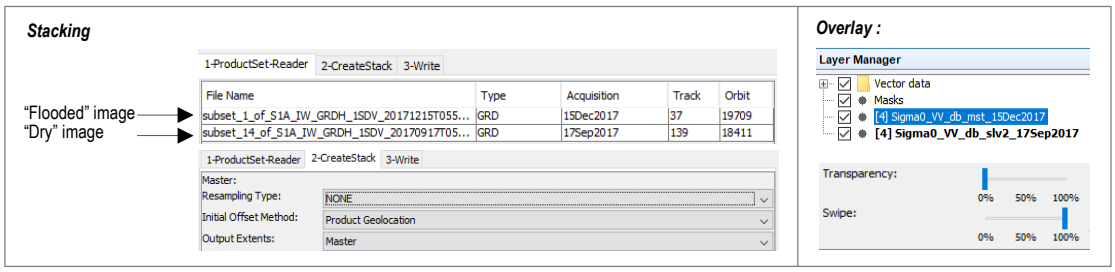

Seen in the stacking steps that two images: flooded and dry are pile up into one stack file as geolocation product. The stacked images were afterwords overlaid each other for clearer flood monitoring display (used transparancy and swipe option) demonstrated the areas that changed due to inundation when the flooding occured

Figure 2. 25. Stacking and Overlay on Sentinel-1 Images

Compilation of the two images was applied resulted in two images that were piled in one display, so it is more reasonable to demonstrated the change occurred due to flooding event as illustrated in Figure 2.26 below.

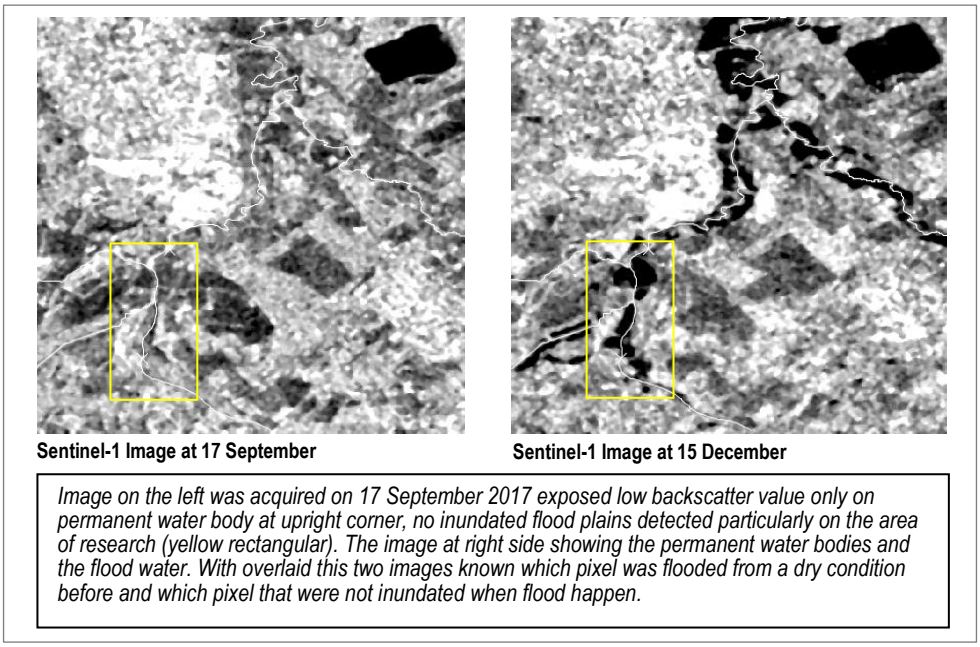

Figure 2. 26. The Sentinel-1 Images Stacked from Dry and Flooded Event

From Figure 2.26 above, known that the flooded image was acquired on 15 December 2017 when the flood happenned as observed at the research area on 14 December 2017, where the flood plains were inundated (Figure 2.27). Supported the stacked process applied above, fieldwork documentation showed the area at the dry time and the flooded event. These photos as illustrated in Figure 2.27 below were validated the dry condition and the flood condition captured by the Sentinel-1 SAR images.

Figure 2. 27. Field Work Documentation when The Area was Dry and when it was Flooded

Noted that stacking and overlay between two images above was intended to make an RGB colour composite for distinguishing flooding water with permanent water bodies and another land cover which are not water bodies. The RGB colour composite process illustrated in Figure 2.28 below

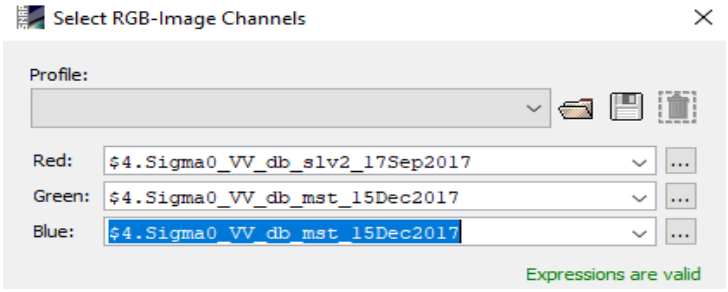

The RGB composite formation, shown the red channel is filled with sigma0_VV_db band of dry image while the green and blue band filled with sigma0_VV_db band of flooded image. This composite result a certain color differences of backscatter between permanent water bodies and the flooded water, and also difference with other land cover which are not water objects.

Figure 2. 28. RGB Colour Composite Formation

The reason behind the colour composite formation as seen in Figure 2.28 above is the differences on backscatter responses from two images has brought consequences in the composite image affected by different bands that filled the RGB channels. Low backscatter of the flooded area at the flooded image made the green and blue channel have low backscatter as well, consequences green and blue colours would not appear in composite for represented the flooded area. On the other hand, Red channel that filled with dry image band constantly gave high backscatter responses in the composite that cause the flooded area that was not inundated in the dry image, showing a high response in the red colour in the composite image. RGB Colour composite was generated as shown in Figure 2.29 below, showing the contrast red colour as backscatter value from the flood water.

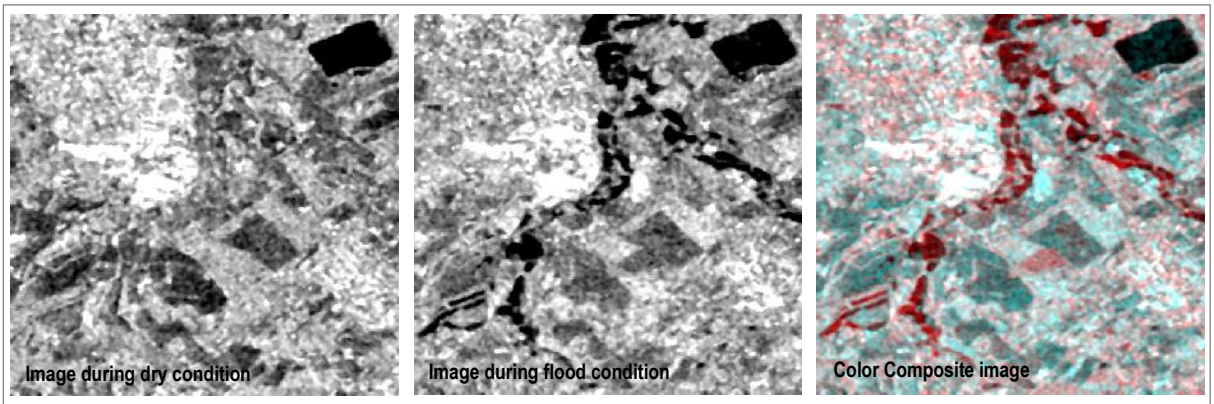

The composite result shown that permanent water body at the right is constantly appear black as well as in the dry and flooded image. This similar backscatter value is caused by uniform low backscatter responses of the exact object reflected from dry and flooded images in red, green, and blue band at the exact pixel. Seen in the dry image no inundated area detected, means no low backscatter responses is expected. In contrary at flooded image, inundated areas were detected as black/dark due to low backscatter responses. Red colour represented the flooded water at the composite image appeared due to the exact inundated pixels was filled with the red colour before it inundated at the flooded image (low backscatter). The grey tones is represented the same backscatter responses from red, green, and blue. Gradually cyan colors is related to the ground covers that may not related with the flood.

Figure 2. 29. Result of Colour Composite Image from Dry and Flooded Image

Based on the colour composite image in Figure 2.29 above, backscatter value of flood water has clearly distinguished from the permanent water body and from another land cover neither. As mention above that red colour indicated the flood water, then the inspection the red colour pixel value was later applied. The

composite result led to the certain threshold value of flood water that used to all flooded time-series images. The backscatter threshold value determination was done as illustrated in Figure 2.30 below.

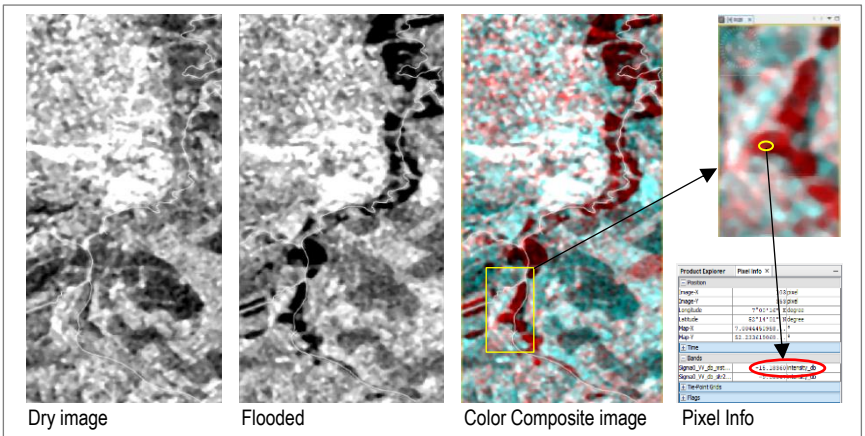

Figure 2. 30. Backscatter Value Determination for Flooded Pixel

As seen in Figure 2.30 where the "suspected" backscatter value of flood water was indicated, the pixel value of *-15* was later applied for flood water pixel determination at all flooded images *sigma0_VV* bands. Noted that this pixel value was stated after numbers of trials of using different values as a flood threshold value and being compared to different flooded images.

As addressed the flood threshold value of sigma_VV_db was -15 db, this value was then applied in the *bandmath* to all flooded images. The threshold value was applied in bandmath with the expression: ***if Sigma0_VV_db <-15 then one else NaN*** means that every pixel value *below -15* classified as *1* and the *other value* is *Not a Number*. Based on the math expression above, the resulting image displayed in binary values. Value 1 means flooded that appeared in white and non-flooded is not represented by a number that appeared in black (as the background colour). However, noticed that Sentinel-1 images have two different orbit direction, ascending and descending that affected the backscatter responses received by the satellite (Béjar-Pizarro et al., 2017; Makynen & Karvonen, 2017; Reiu, Zalite, Kaupo, & Phd, 2017). Referring to that, the threshold value -15 db was tested to applied as a flood threshold value to two images with different orbit direction/pass as illustrated in Figure 2.31 below.

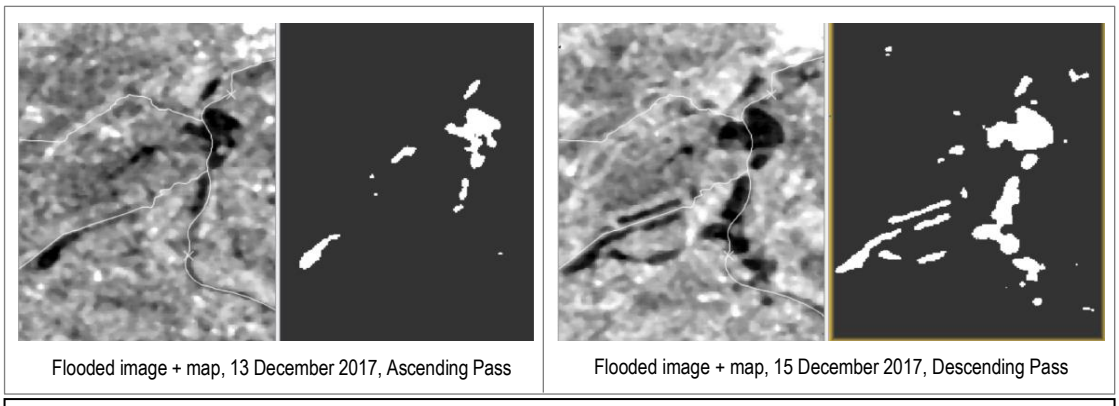

Figure 2. 31. Sentinel-1 Flooded Images with Ascending and Descending Pass

Comparing the flooded image and the flood maps from Figure 2.31 above, known that threshold value that applied to the different orbit pass of the images was equally impacted the flood extent retrieval in both images.

There were 46 Sentinel-1 images categorised as flooded in this research. All the flooded images were terrain corrected, subsetted, speckle filtered, and flood pixel threshold determined. Speckle filter and flood threshold value were applied in parallel using a batch processing. This process was applied by using the model graph that was built for filtering and band math in one process. Batch processing executed the series of tasks in one program and avoided the manual intervention on every single task, so the result was retrieved efficiently. This batch processing was applied to all flooded images to generating 46 flood maps of the research area from October 2014 to December 2017. The graph that shown batch processing was applied for flood maps generation which is shown in Figure 2.32 below.

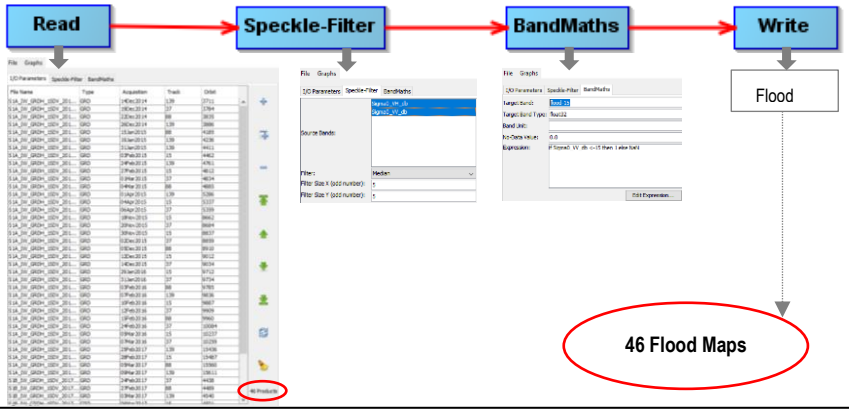

Seen that calibrated (db) sigma0_VH and sigma0_VV bands were filtered with median 5x5, and flood treshold value -15 was input for flood extent value to of sigma0_VV band of each image in band math. Each flood map named with flood-15. This batch processing resulted 46 flood maps

Figure 2. 32. Flood Maps Generation Process in Batch Processing

As illustrated in Figure 2.32 above, the 46 flood maps were generated as the results of SAR imagery application for flood detection. After the flood maps generated, *the second step* was water level estimation by merging the flood extent polygon with the DEM retrieved from UAV. Serial flood maps were later plotted on the UAV's DEM to quantify the water level of the inundated area as seen from Figure 2.33 below.

The water level measurement from SAR images were done by masking the generated UAV's DEM with the flood maps generated. The pixel value in red square is the estimated water level that were measured from UAV's DEM platform, when the Zoekerbrug insitu measurement station were inundated by flood.

Figure 2. 33. Water Level Estimation from SAR Images Flood Map

As seen from Figure 2.33 above, known how many times the certain area/points/pixels were inundated in 46 flooding events estimated with Sentinel-1 images used. Through these inundated area/points/pixels from flood images, the validation was applied with the in-situ water level measurement used. There were two water level measurement stations in the captured area, Weerstbrug at the upper part and Zoekerbrug Station at the lower part of the channel. These two measurement stations have recorded the discharge water level of the river in every one hour, which was a reliable reference for water level estimation from 12 days revisit time of Sentinel-1 SAR images.

The method to estimate the water level at the Zoekerbrug Station was done by delineating the area of the flood extent detected from SAR image and overlaying the flood polygon on the UAV's DEM platform. The flood extent polygon were used as a mask on the UAV's DEM to retrieve the water level of a particular flood event. As addressed that the Zoekerbrug Station's point was inundated in a numbers of flood maps, and later the flood polygon border from every flood map was overlaid on the UAV's DEM. There was one point/coordinate chosen from the flood polygon of every flood map that located at the Zoekerbrug in-situ water level measurement point. The flood water level of this particular point was determined by looked at the elevation measured with UAV's DEM platform. This method was effectively estimated the water level of the flood water at Zoekerbrug station point as presented in the result. Therefore, the validation was later applied to point where the water level in-situ measurement inundated by the flood at Zoekerbrug in-situ measurement station.

3. RESULTS

The research has been conducted in three consecutive processes as structured in research method. Every process has generated the results that constructed milestones for obtaining the main research objective.

3.1. UAV's Image Acquisition and Processing

The flight for image acquisition was conducted on 15 September 2017 on the part of Dinkel River segment between Glane and Losser. The image acquisition resulted in 683 images in total, captured in three flights. The UAV flights at 50 meters above the Dinkel man-made channel covered the river, the banks and a part of the floodplains at the left and right bank along this section. The forward overlap of the images was 80% as well as side overlap.

There were seven distributed GCPs used for the image georeferencing which each point has mean errors of geolocation in three coordinate directions (X,Y,Z), as shown in Table 3.1 below.

Table 3. 1. GCPs Accuracies in Images Georeferencing Process

GCP's Coordinates :

ID	Latitude	Longitude	Altitude
GPS0001	52,23220	7,00632	34,8910
GPS0002	52,23217	7,00635	35,4400
GPS0004	52,23236	7,00556	35,5330
GPS0005	52,23240	7,00554	35,7440
GPS0010	52,24271	7,00895	34,8600
GPS0012	52,24312	7,00819	34,4520
GPS0017	52,24434	7,00820	34,6040

7 GCPs coordinates measured with RTK-GPS method.

Localisation Accuracy :

GCP Name	Accuracy XY/Z [m]	Error X [m]	Error Y [m]	Error Z [m]	Projection Error [pixel]	Verified/Marked
GPS0001 (3D)	0.020/ 0.020	0.037	0.030	0.104	0.806	22 / 22
GPS0002 (3D)	0.020/ 0.020	-0.009	-0.035	-0.091	0.519	20 / 20
GPS0004 (3D)	0.020/ 0.020	-0.010	0.017	-0.025	0.737	23 / 23
GPS0005 (3D)	0.020/ 0.020	-0.019	-0.011	0.010	0.590	22 / 22
GPS0010 (3D)	0.020/ 0.020	0.038	-0.019	-0.011	0.286	6 / 6
GPS0012 (3D)	0.020/ 0.020	-0.039	0.024	0.011	0.368	14 / 14
GPS0017 (3D)	0.020/ 0.020	0.002	-0.009	-0.001	0.247	4 / 4
Mean [m]		0.000224	-0.000438	-0.000403		
Sigma [m]		0.026266	0.022377	0.053287		
RMS Error [m]		0.026267	0.022381	0.053289		

Georeferenced accuracy in X,Y,Z direction and in pixel projection error for each GCPs marked on the images, showing RMSE of the georeferenced result and numbers of matched tie points marked in overlap images.

As seen in Table 3.1 above, the RMS Error of the georeferenced process X=0.026, Y=0.022, and Z=0.053 demonstrated acceptable accuracies of the georeferenced image block. The errors also projected in pixels, showed that the biases were less than 1 pixel (2cm x 2cm) for each tie points. The RMS Error values (in meters) proved the fact that the bundle block image was successfully oriented.

Initial processing that has been applied demonstrated the effects of these GCP's position to the area surrounding where the points have plotted. The area where the GCPs were placed has small offset compare with the area with no GCP. This was indicated the area that needed for GCPs so that the additional points could be placed to improve the resulting quality. These distributed tie points contributed well to image orientation result, which has assessed trough uncertainty ellipses, showing the offset between initial and computed positions of images and GCP's, as illustrated in Figure 3.1 below.

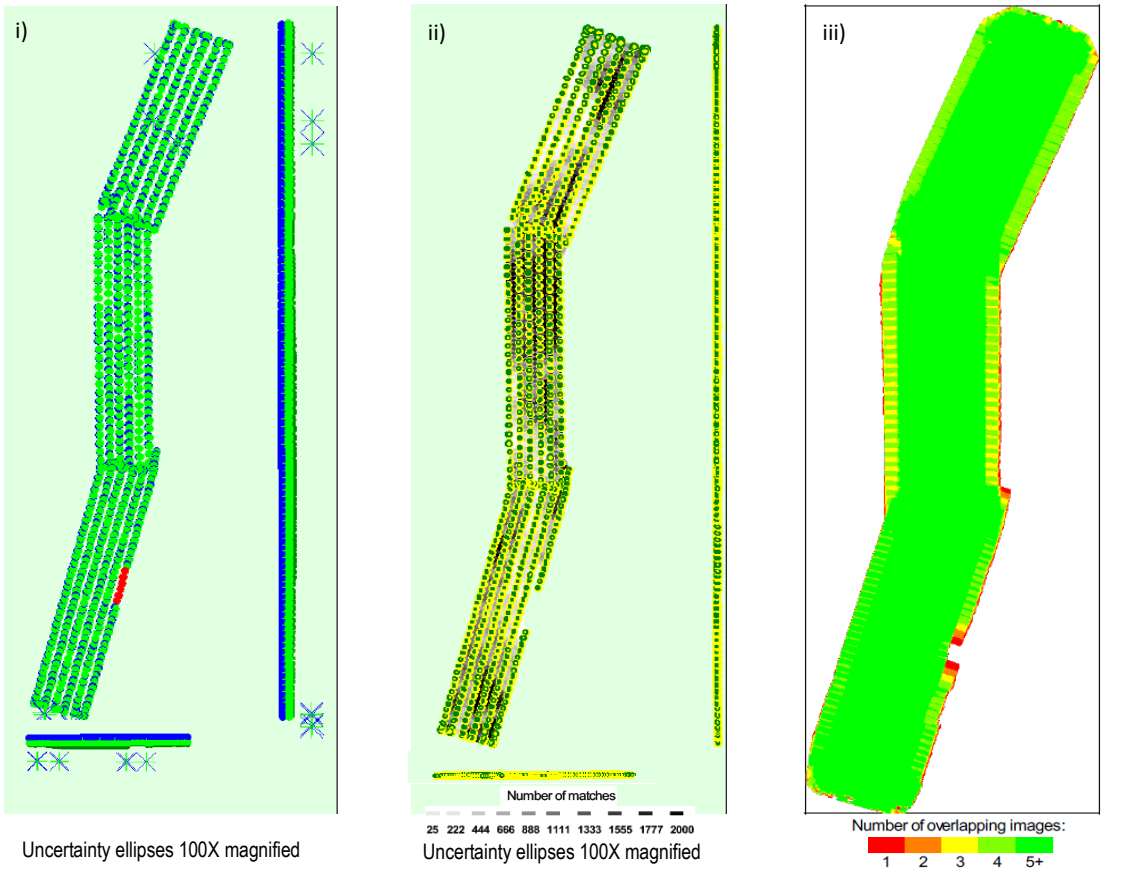

Figure i) *revealed offset between initial (blue dots) and computed (green dots)of image positions,also seen the offset between the GCPs initial positions (blue crosses) and their computed positions (green crosses) from the top-view (XY plane), front-view (XZ plane), and side-view (YZ plane). Red dots indicated the uncalibrated images position. Dark green ellipses indicated the relative camera position uncertainties of the bundle block adjustment result.*

Figure ii) *shown computed image positions with links between matched images. Dark ellipses at the back indicated the number of matched 2D keypoints between the images. Bright links indicated weak links and required manual tie points or more on images.*

Figure iii) *illustrated the number of overlapping images computed for each pixel of the orthomosaic. Red and Yellow areas indicated low overlap for which poor results were generated. Green areas indicated an overlap of more than 5 images for every pixel. Visually, numbers of overlapping images were sufficiently robust in this research.*

Figure 3. 1. Offset between Initial and Computed, Keypoints Matches Link, and Number of Overlapping Images

The Figure 3.1 above illustrated the quality assessment of image processing where GCP's role was crucial. The contribution of evenly distributed GCPs was critical for generated maximum quality of the point cloud. Ray cloud (first point cloud) quality was improved based on those assessments applied (Figure 3.2.). Improving ray cloud has generated a more dense point cloud, and later were played the main role on the creation of the Digital Surface Model (DSM).

The Image processing has resulted in the high dense point cloud which has been transformed to Digital Surface Model and the orthophoto of the area, as illustrated in Figure 3.2 below.

Figure i) *Shown the high density point cloud as a result of image processing. There were few "blank area", which based on the visual observations on the field known as the area of maize crops and high trees/bushes.*

Figure ii) *Illustrated DSM product in LAS file, appeared the blank areas that were represented the high density vegetation leaves. There are colors that were represented the elevation, informed the different land covers from ground, low vegetation (grass) to a higher elevation object associated with trees leaves.*

Figure iii) *is the orthophoto of the area, showing the full coverage captured by the flights. The small blank area (red circle) is the consequences of the 6 uncalibrated images at processing step, 99,12 % (677 out of 683) images are calibrated.*

Figure 3. 2. Image Processing Results : i) Point clouds, ii) DSM in LAS file format, iii) Orthophoto

DSM LAS file resulted as seen in Figure 3.2 above, was later processed for the ground class extraction and conversion to terrain platform known as DEM.

3.2. DSM to DEM Conversion

DSM retrieved from the UAV flights was later converted to DEM. The conversion was applied in steps that were structured in the research method. As composed in the research method, there were two sets of UAV's DEM generated based on different ground filtered applied. Addressed as well in the research objective that the DEM utilization purposes were determined the level of expected accuracy, then a different level of accuracy was generated and compared for hydraulic modeling purpose. These DEMs were later proposed to be used for the water level estimation with SAR images flood extent.

Noted that the UAV's DEM generated in 2cm grid resolution accuracy that was referred to 2.03cm GSD of UAV's image considered as a very small grid, later this 2cm grid size DEM was aggregated into 40cm grid resolution. For showing the difference between surface and the terrain, DSM was also created with the same steps as the DEM conversion showed, only there was no *ground class (class 2)* extraction on the filtering step. The comparison of DEM generated from *extra fine nature*, *modification on filtering parameter* and DSM all in 2cm grid resolution/accuracy illustrated in Table 3.2 below.

Table 3. 2. Comparison on 2cm Accuracy of the Generated DEM and DSM

Process	DEM 2 cm accuracy		DSM 2 cm accuracy
	Extra Fine	Filtering: Offset,Spike, & Std Dev	
lasground	*lasground –lof file_list.14332.txt –cores 4 –no_bulge –nature –extra_fine –odir c:\Hariady_Thesis\LAS_file\02_lasground _extra" –odix "_g" –olaz*	*lasground –lof file_list.10220.txt –cores 4 –bulge 0 –offset 0.02 -spike 0.3 –stddev 2 –odir c:\Hariady_Thesis\LAS_file\02_llasground_ withparameter" –odix "_gp" –olaz*	no conversion to ground class
las2dem	*las2dem –lof file_list 9496.txt –keep_class 2 –use_tile_bb –odir "c:\Hariady_Thesis\LAS_files\03_las2de m_extra" –odix "_dtm" –obil –step 0.02 –cores 4*	*las2dem –lof file_list 10156.txt –keep_class 2 –use_tile_bb –odir "c:\Hariady_Thesis\LAS_files\03_las2dem_ withparameter" –odix "_dtmp" –obil –step 0.02 –cores 4*	*las2dem –lof file_list 12384.txt –step 0.02 –kill 200 -use_tile_bb –odir "c:\Hariady_Thesis\LAS_files\03_las2dem _dsm" –odix "_dsm" –obil –cores 4*
lasgrid	*lasgrid –lof file_list 10168.txt –merged –step 0.02 –odir "c:\Hariady_Thesis\LAS_files\04_lasgrid_ extra" –o "merged_2cm_nooptionx.bil"*	*lasgrid –lof file_list 7646.txt –merged –step 0.02 –odir "c:\Hariady_Thesis\LAS_files\04_lasgrid_wi thparameter" –o "merged2cm_parameter.bil"*	*lasgrid –lof file_list 1216.txt –merged –step 0.02 –odir "c:\Hariady_Thesis\LAS_files\04_lasgrid_ dsm"–o "merged_dsm.bil"*
Result	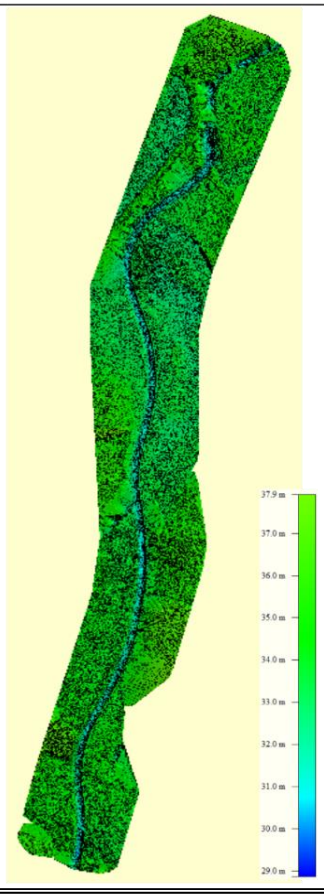	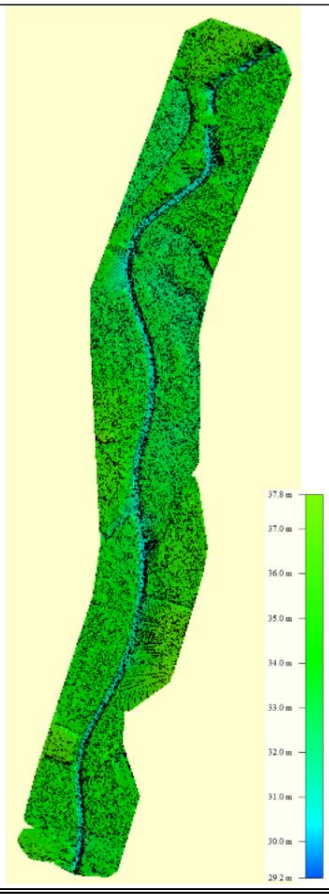	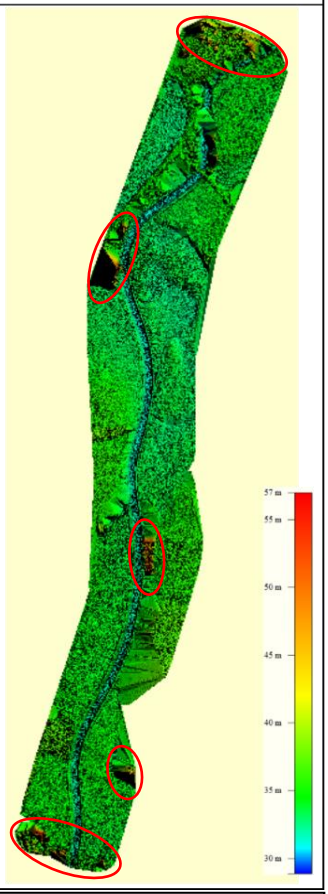

Seen the differences on elevation above sea level between the DEM and DSM, indicated that certain points classified as surfaces were not taken into account in the ground class represented with the DEM. At the DSM view, noticed that the elevation reach 57 meter high displayed with reddish colors on the land surfaces. From the inspection, known that these reddish color points are classified as high vegetation and building.

At the generated DEM view, shown the highest elevation is 37 meters indicated that the point classes with non-ground classes at the surface had been cut out from the ground.

Result comparison on the DEMs and DSM in the 40cm aggregation grid resolution were also applied as illustrated in Table 3.3 below.

Table 3. 3. Comparison on 40 cm Accuracy of Generated DEM and DSM

Process	DEM 40 cm accuracy		DSM 40 cm accuracy
	Extra Fine	**With Filtering Parameter**	
lasgrid	*lasgrid –lof file_list 10168.txt –merged –step 0.4* –elevation –average –odir *"c:\Hariady_Thesis\LAS_files\05_resolution_reduction_dtmx" –o "merged_40cm_averagex.bil"*	*lasgrid –lof file_list.7648.txt –merged –step 0.4* –odir *"c:\Hariady_Thesis\LAS_files\05_resolution_reduction_withparameter" –o "merged_parameter40cm.bil"*	*lasgrid –lof file_list 1224.txt –merged –step 0.4* –odir *"c:\Hariady_Thesis\LAS_files\05_resolution_reduction_dsm"–o "merged_40cmdsm.bil"*
Result	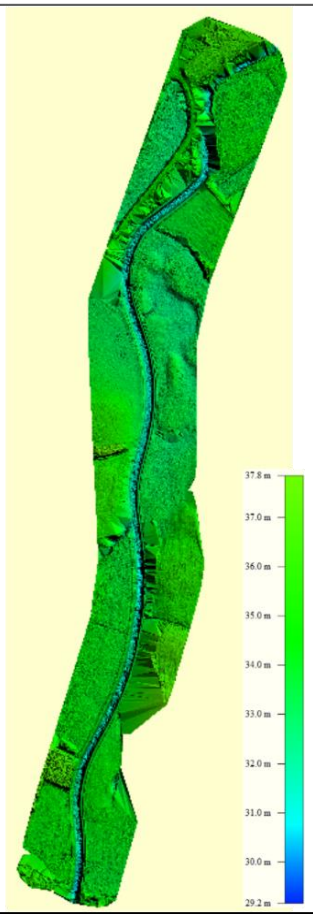	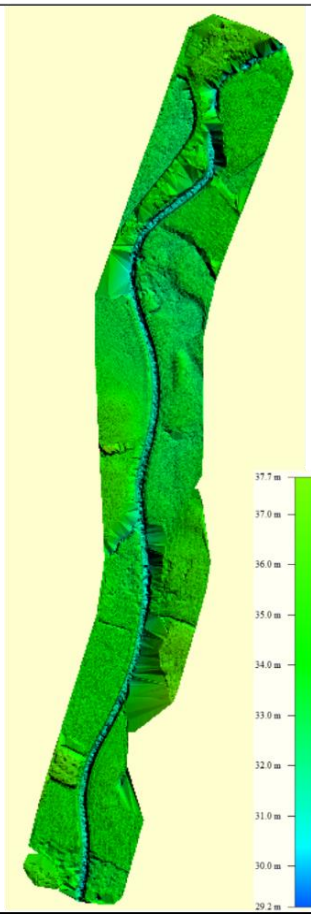	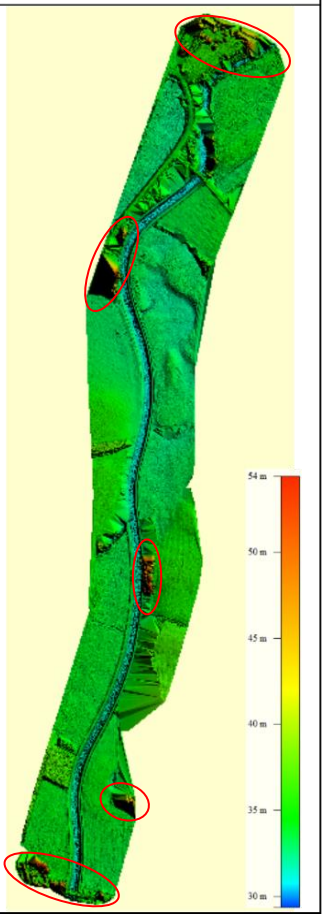

Seen the the elevation models looks "smoother" due to grid size aggregation. the elevation range different between the DEM and DSM were different as addressed in 2cm comparison as well. At the DSM view, noticed that the elevation range reach 54 meter displayed with reddish colors on the higher land cover, known the objects are high trees/shrubs and building roof.

37 meters elevation range at the generated DEM view, were similar with elevation range of DEM in 2cm accuracy, shown the non-ground classes at the surface had been filtered out.

The generated DEMs were later validated with reference points that were retrieved from RTK GPS measurement. The Validation was done by comparing the Z coordinate (elevation) of each reference points above with the Z coordinate of the same points from the different set of DEMs. The comparison of Z coordinate was applied to DEMs produced with different ground filtering (2 DEM), different accuracies (2 DEM), DEM from AHN2 (1 DEM), and the reference points from RTK-GPS measurement as a reference. There were five sets of DEMs were compared and validated with the RTK GPS reference points.

Each set of DEM and DSM was compared on reference points taken from left and right banks in parallel. The reference points were measured at the left (red triangle) and right (yellow triangle) banks of the channel and plotted at orthophoto from UAV image processing, as illustrated in Figure 3.3 below.

Figure 3. 3. RTK GPS Points Distribution

From the comparison, every DEM set was assessed based on RMSE value to the reference points. The DEM-reference points of Z coordinate comparison with the smallest RMSE value would be chosen. This validation process was expected to outcome one set of DEM that would be used for flooding water level estimation.

At the validation, also plotted the elevation of the reference points measured at DEM AHN2 *(Actueel Hoogtebestand Nederland)* with 50 cm resolution. This DEM was retrieved from a laser aircraft (lidar), known

as a robust method for 3D altitude information retrieval to cover every square meter to 50 cm² in the Netherlands. DEM AHN2 used as a main digital elevation model parameter for flood mitigation planning and water management by *Rijkswaterstaat* (Public Works Ministry) and *Waterschap* (Water Board) of the Netherlands. The comparison was to show that the generated UAV's DEM is comparable with the reliable similar product so that the UAV's DEM also could be utilized for hydraulics modeling purposes. The validation illustrated in Figure 3.4 below were applied using the reference points from the RTK-GPS measurement points.

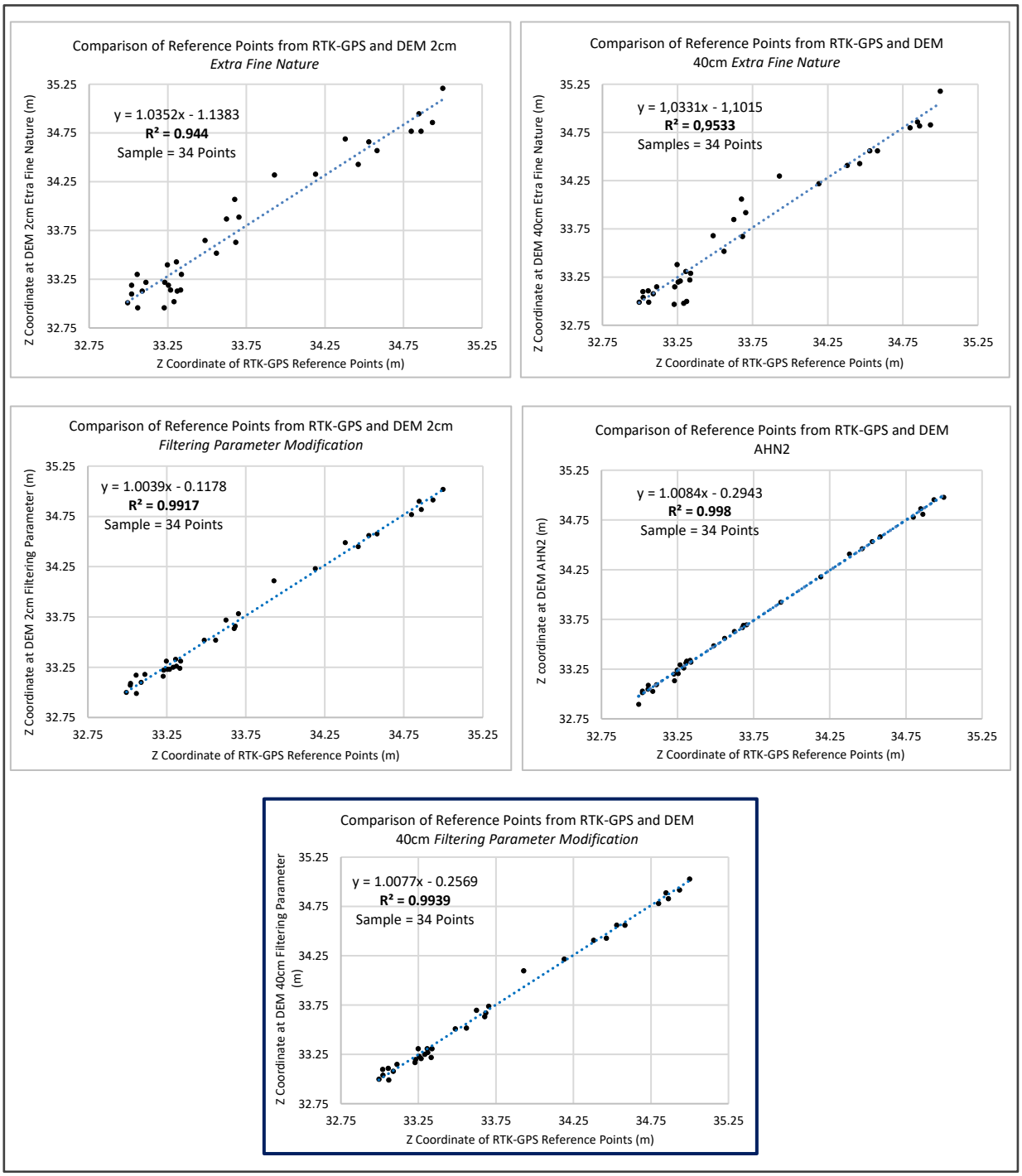

Figure 3. 4. Validation of Elevation Models at the Reference Points

Figure 3.4 above shown the DEM from AHN2 was shown the closest relation with the terrain which was 99.8%. However, the DEM set generated from ground filtering parameter modification was also shown a reliable validation result with 99.39% correlation to the reference terrain.

From the validation of DEMs above, RMSE was calculated from each model with the result presented in Table 3.4 below.

Table 3. 4. RMSE Values of Elevation Models to Reference Points

Elevation Models	RMSE (m)
DEM 2cm *Extra Fine Nature*	0.1743
DEM 40cm *Extra Fine Nature*	0.1526
DEM 50cm AHN2	0.0318
DEM 2cm *Ground Filtering Modification*	0.0617
DEM 40cm *Ground Filtering Modification*	0.0522

Shown in Table 3.4 above that the comparison of elevation model generated to reference points, DEM AHN2 given the smallest root mean square errors. This is reasonably considering that the method of retrieval with lidar has a significant advantage due to powerful penetration of laser to going through the dense objects such as trees canopy, bushes, and maize which were founded as one of the obstacles of DEM Retrieved by UAV. That advantage of laser application contributed critically for the dense point cloud generation with more certain surfaces classes due to three different back responses of laser signal from the earth. However, with plentiful of modifications on ground filtering parameter, the reliable result of DEM was produced in this research as illustrated from the RMSE table above. DEMs that were resulted from filtering parameters are presented in two different resolution given the RMSE 6.17 cm for 2cm resolution and 5.22 cm for 40cm resolution. The 40cm x 40cm aggregated resolution was diminished the coarseness of the elevation model due to the expanded grid size of the DEM. Considering the validation result on linear regression and RMSE value, added with the fact that 40cm DEM grid sized was very reasonable for hydraulic modeling purposes. Therefore, the DEM with the 40cm resolution was further used for water level estimation.

3.3. Flood Extent Threshold Determination from multi-temporal SAR imagery on the UAV's DEM platform.

The SAR imagery that has been used for generating the flood maps in this research which consists of the Sentinel-1 temporal images with acquisition date from October 2014 to December 2017. Over this period of time, there were 46 Sentinel-1 SAR images identified as flooded images. The flooded images used listed in Table 3.5 below.

Table 3. 5. The list of 46 Flooded Images from December 2014 to December 2017

No	Sentinel-1 Images	Ascquisition Date	Pass	Acqusition End Time
1	S1A_IW_GRDH_1SDV_20141214T054121_20141214T054146_003711_00468C_5FCE	14 December 2014	Descending	05:41:46
2	S1A_IW_GRDH_1SDV_20141219T054931_20141219T055000_003784_004847_65BC	19 December 2014	Descending	05:50:00
3	S1A_IW_GRDH_1SDV_20141222T172442_20141222T172507_003835_004964_EA4A	22 December 2014	Ascending	17:25:07
4	S1A_IW_GRDH_1SDV_20141226T054120_20141226T054145_003886_004A8C_37A4	26 December 2014	Descending	05:41:45
5	S1A_IW_GRDH_1SDV_20150115T172441_20150115T172506_004185_005144_64A6	15 January 2015	Ascending	17:25:06
6	S1A_IW_GRDH_1SDV_20150119T054120_20150119T054145_004236_00526B_6D73	19 January 2015	Descending	05:41:45
7	S1A_IW_GRDH_1SDV_20150131T054119_20150131T054144_004411_005640_E26F	31 January 2015	Descending	05:41:44
8	S1A_IW_GRDH_1SDV_20150203T171625_20150203T171650_004462_005779_9FBE	03 February 2015	Ascending	17:16:50
9	S1A_IW_GRDH_1SDV_20150224T054119_20150224T054144_004761_005E6F_12E3	24 February 2015	Descending	05:41:44
10	S1A_IW_GRDH_1SDV_20150227T171624_20150227T171649_004812_005FB6_D350	27 February 2015	Ascending	17:16:49
11	S1A_IW_GRDH_1SDV_20150301T054929_20150301T054958_004834_006043_AD31	01 March 2015	Descending	05:49:58
12	S1A_IW_GRDH_1SDV_20150304T172416_20150304T172448_004885_00616B_44BC	04 March 2015	Ascending	17:24:48
13	S1A_IW_GRDH_1SDV_20150401T054120_20150401T054145_005286_006AFC_C4BE	01 April 2015	Descending	05:41:45
14	S1A_IW_GRDH_1SDV_20150404T171627_20150404T171652_005337_006C3A_7B1C	04 April 2015	Ascending	17:16:52
15	S1A_IW_GRDH_1SDV_20150406T054930_20150406T054959_005359_006CCE_03BC	06 April 2015	Descending	05:49:59
16	S1A_IW_GRDH_1SDV_20151118T171630_20151118T171655_008662_00C501_EC91	18 November 2015	Ascending	17:16:55
17	S1A_IW_GRDH_1SDV_20151120T054932_20151120T055001_008684_00C5A1_FE21	20 November 2015	Descending	05:50:01
18	S1A_IW_GRDH_1SDV_20151130T171635_20151130T171700_008837_00C9E6_55DE	30 November 2015	Ascending	17:17:00
19	S1A_IW_GRDH_1SDV_20151202T054950_20151202T055015_008859_00CA88_74E0	02 December 2015	Descending	05:50:15
20	S1A_IW_GRDH_1SDV_20151205T172438_20151205T172503_008910_00CBFF_3058	05 December 2015	Ascending	17:25:03
21	S1A_IW_GRDH_1SDV_20151212T171629_20151212T171654_009012_00CEC5_3229	12 December 2015	Ascending	17:16:54
22	S1A_IW_GRDH_1SDV_20151214T054931_20151214T055000_009034_00CF62_02A0	14 December 2015	Descending	05:50:00
23	S1A_IW_GRDH_1SDV_20160129T171627_20160129T171652_009712_00E2DB_3C87	29 January 2016	Ascending	17:16:52
24	S1A_IW_GRDH_1SDV_20160131T054930_20160131T054959_009734_00E382_A766	31 January 2016	Descending	05:49:59
25	S1A_IW_GRDH_1SDV_20160203T172449_20160203T172514_009785_00E4F4_D272	03 February 2016	Ascending	17:25:14
26	S1A_IW_GRDH_1SDV_20160207T054137_20160207T054202_009836_00E667_6C6F	07 February 2016	Descending	05:42:02
27	S1A_IW_GRDH_1SDV_20160210T171632_20160210T171657_009887_00E7E2_F3BE	10 February 2016	Ascending	17:16:57
28	S1A_IW_GRDH_1SDV_20160212T054947_20160212T055012_009909_00E898_33DD	12 February 2016	Descending	05:50:12
29	S1A_IW_GRDH_1SDV_20160215T172426_20160215T172451_009960_00EA11_6A30	15 February 2016	Ascending	17:24:51
30	S1A_IW_GRDH_1SDV_20160224T054930_20160224T054959_010084_00EDB7_2C9E	24 February 2016	Descending	05:49:59
31	S1A_IW_GRDH_1SDV_20160305T171633_20160305T171658_010237_00F1FA_DD17	05 March 2016	Ascending	17:16:58
32	S1A_IW_GRDH_1SDV_20160307T054948_20160307T055013_010259_00F2A6_3E5C	07 March 2016	Descending	05:50:13
33	S1B_IW_GRDH_1SDV_20170224T054900_20170224T054925_004438_007B8A_58ED	24 February 2017	Descending	05:49:25
34	S1A_IW_GRDH_1SDV_20170225T054126_20170225T054151_015436_01956B_293D	25 February 2017	Descending	05:41:51
35	S1B_IW_GRDH_1SDV_20170227T172401_20170227T172426_004489_007D03_4A39	27 February 2017	Ascending	17:24:26
36	S1A_IW_GRDH_1SDV_20170228T171630_20170228T171655_015487_0196F9_00AF	28 February 2017	Ascending	17:16:55
37	S1B_IW_GRDH_1SDV_20170303T054041_20170303T054106_004540_007E86_8614	03 March 2017	Descending	05:41:06
38	S1A_IW_GRDH_1SDV_20170305T172447_20170305T172512_015560_019933_85FB	05 March 2017	Ascending	17:25:12
39	S1B_IW_GRDH_1SDV_20170306T171546_20170306T171611_004591_008004_C9EE	06 March 2017	Ascending	17:16:11
40	S1B_IW_GRDH_1SDV_20170308T054900_20170308T054925_004613_0080A8_DC3D	08 March 2017	Descending	05:49:25
41	S1A_IW_GRDH_1SDV_20170309T054126_20170309T054151_015611_019AB8_FC83	09 March 2017	Descending	05:41:51
42	S1B_IW_GRDH_1SDV_20170311T172401_20170311T172426_004664_008222_B240	11 March 2017	Ascending	17:24:26
43	S1A_IW_GRDH_1SDV_20171213T171650_20171213T171715_019687_02174D_E1AF	13 December 2017	Ascending	17:17:15
44	S1A_IW_GRDH_1SDV_20171215T055004_20171215T055029_019709_0217FC_B703	15 December 2017	Descending	05:50:29
45	S1B_IW_GRDH_1SDV_20171216T054104_20171216T054129_008740_00F8CB_AE47	16 December 2017	Descending	05:41:29
46	S1B_IW_GRDH_1SDV_20171219T171555_20171219T171620_008791_00FA65_C386	19 December 2017	Ascending	17:16:20

Resulted flood maps were later overlaid in one layer to generate the flood frequency that was happened in the area based on flood detection from SAR imagery, as illustrated in Figure 3.5 below

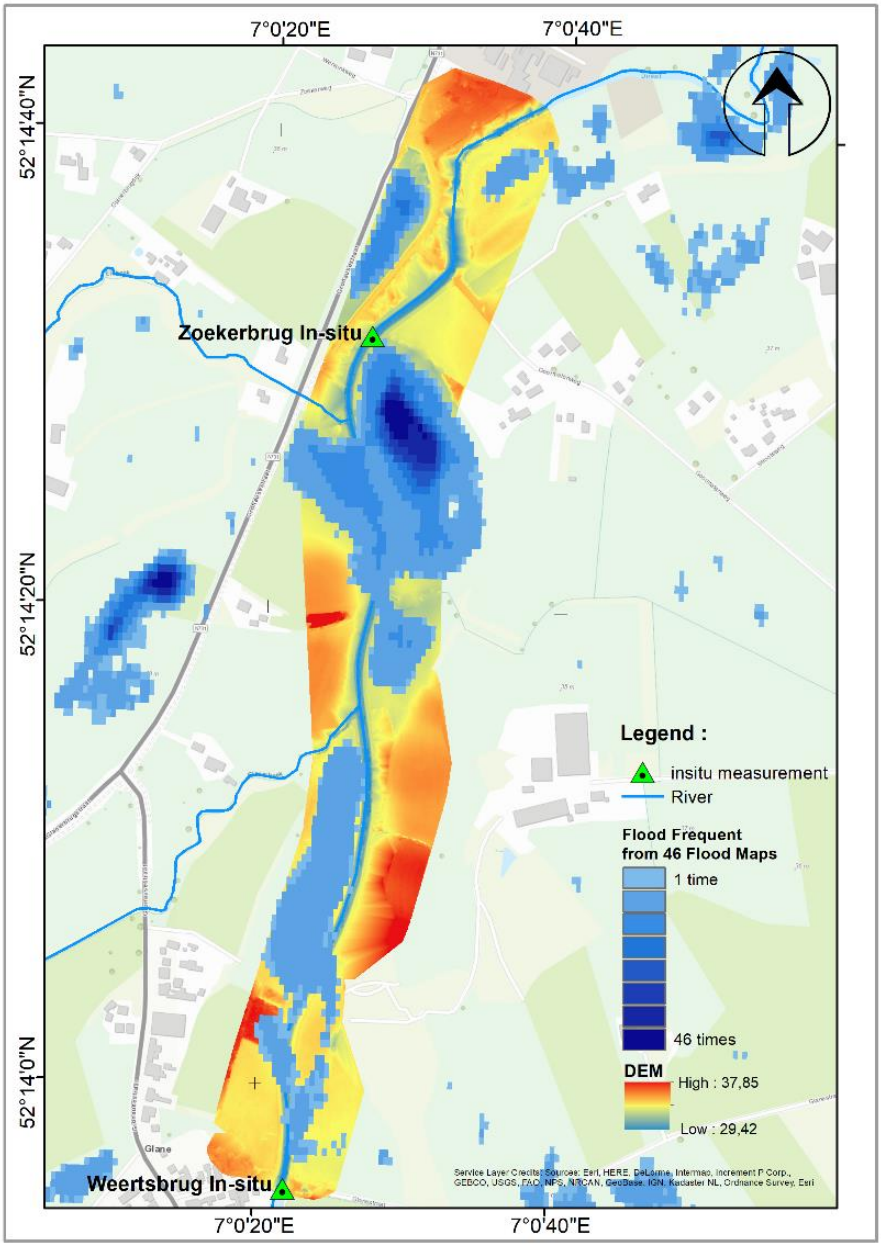

Figure 3. 5. Flood Frequency Map based on Flood Detection on SAR Imagery October 2017 to December 2017

Referring the flood frequency map in Figure 3.5 above, noticed that the size of the inundated area was diverse on every flood event and there were no flood inundation events at The Weertsbrug in-situ measurement station. Therefore the validation of the water level between in-situ measurement at The Zoekerbrug station and water level from SAR imagery was applied based on flood map when the in-situ measurement instrument/station was inundated by flood. As seen in Figure 3.5 above, the water level of the inundation area/point was measured at the flood map when The Zoekerbrug station inundated with the flood by the time it was captured by the Sentinel-1 image.

Numbers of images with the similar condition at this in-situ measurement station and the water level measured were listed in Table 3.6 below.

Table 3. 6. Water Level Measurement from SAR Images Flood Maps and In-situ Measurement

Ascquisition Date	Acqusition End Time	Zoekerbrug In-situ (m)	SAR at Zoekerbrug UAVs DEM (m)	SAR at Zoekerbrug_AHN2 DEM (m)
14 December 2014	05:41:46	33.436	33.464	33.454
19 December 2014	05:50:00	33.043	not-inundated	not-inundated
22 December 2014	17:25:07	33.134	not-inundated	not-inundated
26 December 2014	05:41:45	32.816	not-inundated	not-inundated
15 January 2015	17:25:06	33.403	33.414	33.410
19 January 2015	05:41:45	32,684	not-inundated	not-inundated
31 January 2015	05:41:44	33.729	33.860	33.788
03 February 2015	17:16:50	33.209	not-inundated	not-inundated
24 February 2015	05:41:44	32.781	not-inundated	not-inundated
27 February 2015	17:16:49	33.237	not-inundated	not-inundated
01 March 2015	05:49:58	32.696	not-inundated	not-inundated
04 March 2015	17:24:48	32.968	not-inundated	not-inundated
01 April 2015	05:41:45	33.837	33.900	33.828
04 April 2015	17:16:52	33.195	not-inundated	not-inundated
06 April 2015	05:49:59	32.582	not-inundated	not-inundated
18 November 2015	17:16:55	No Data	not-inundated	not-inundated
20 November 2015	05:50:01	No Data	not-inundated	not-inundated
30 November 2015	17:17:00	No Data	33.560	33.577
02 December 2015	05:50:15	No Data	33.620	33.714
05 December 2015	17:25:03	No Data	not-inundated	not-inundated
12 December 2015	17:16:54	No Data	not-inundated	not-inundated
14 December 2015	05:50:00	No Data	not-inundated	not-inundated
29 January 2016	17:16:52	No Data	not-inundated	not-inundated
31 January 2016	05:49:59	No Data	34.100	34.118
03 February 2016	17:25:14	No Data	not-inundated	not-inundated
07 February 2016	05:42:02	No Data	not-inundated	not-inundated
10 February 2016	17:16:57	No Data	33.579	33.668
12 February 2016	05:50:12	No Data	not-inundated	not-inundated
15 February 2016	17:24:51	No Data	not-inundated	not-inundated
24 February 2016	05:49:59	No Data	not-inundated	not-inundated
05 March 2016	17:16:58	No Data	not-inundated	not-inundated
07 March 2016	05:50:13	No Data	not-inundated	not-inundated
24 February 2017	05:49:25	No Data	33.710	33.722
25 February 2017	05:41:51	No Data	33.570	33.681
27 February 2017	17:24:26	No Data	not-inundated	not-inundated
28 February 2017	17:16:55	No Data	not-inundated	not-inundated
03 March 2017	05:41:06	No Data	not-inundated	not-inundated
05 March 2017	17:25:12	No Data	not-inundated	not-inundated
06 March 2017	17:16:11	No Data	not-inundated	not-inundated
08 March 2017	05:49:25	No Data	not-inundated	not-inundated
09 March 2017	05:41:51	No Data	33.709	33.713
11 March 2017	17:24:26	No Data	not-inundated	not-inundated
13 December 2017	17:17:15	No Data	33.700	33,735
15 December 2017	05:50:29	No Data	34.140	34.131
16 December 2017	05:41:29	No Data	33.990	34.079
19 December 2017	17:16:20	No Data	not-inundated	not-inundated

From Table 3.6 above, known that water level measurement from the SAR images flood maps was done using two DEM platform; 40cm resolution of UAV's DEM and 50cm resolution of AHN2 DEM. However, some of the in-situ measurement water level data were not completely received in this research. Therefore, the comparison of the water level measurement from three different sources above was applied based on the data completeness on every source.

The comparison of in-situ measurement, when inundated by the flood, compare with water level measurement from DEMs platform above were done as illustrated in Table 3.7 below.

Table 3. 7. Water Level Measurement at Zoekerbrug Station

Ascquisition Date	Zoekerbrug In-situ (m)	Zoekerbrug UAVs DEM (m)	Zoekerbrug_AHN2 DEM (m)
14 December 2014	33.436	33.464	33.454
15 January 2015	33.403	33.414	33.410
31 January 2015	33.729	33.860	33.788
01 April 2015	33.837	33.900	33.828
30 November 2015	No Data	33.560	33,577
02 December 2015	No Data	33.620	33,714
31 January 2016	No Data	34.100	34,118
10 February 2016	No Data	33.579	33,668
24 February 2017	No Data	33.710	33,722
25 February 2017	No Data	33.570	33,681
09 March 2017	No Data	33.709	33,713
13 December 2017	No Data	33.700	33,735
15 December 2017	No Data	34.140	34,131
16 December 2017	No Data	33.990	34,079

Based on the list in Table 3.7 above, assessment of water level measured at the UAV's DEM was applied with comparing to AHN2 DEM platform and the in-situ measurement as the reference, at the dates when data were complit from both side (see the blue square border above). The accuracy assessment at Figure 3.6 below demonstrated the reliability of UAV application for retrieving accurate DEM to be used as topography parameter for estimating the flood water level extent value.

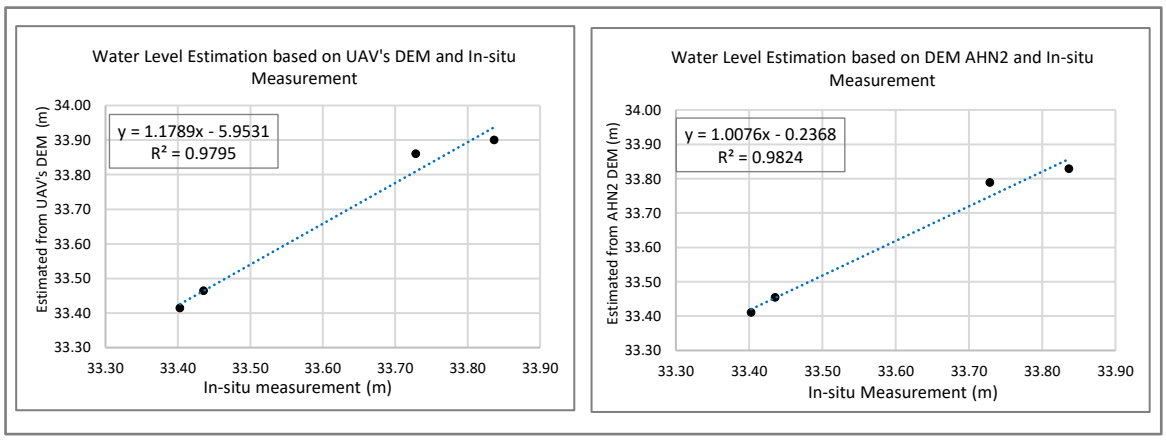

Figure 3. 6. Accuracy Assesment of generated DEM application for flood water level estimation

From Figure 3.6 above, it is known that the UAV's DEM 40cm resolution application for water level estimation has resulted 97.95% correlated with water level from in-situ measurement. Supported the addressed correlation above, below is the RMSE values of using the DEM from UAV and DEM from AHN2 to determining the threshold for water level at the inundated area around Zoekerbrug station.

Table 3. 8. RMS Errors of Water Level from UAV's DEM and DEM AHN2 compared with In-situ Measurement

Elevation Model	RMSE
Estimated on UAV's DEM	0.0672
Estimated on AHN2 DEM	0.0314

Validation result designated by RMSE value in Table 3.8 above, showing that using the DEM retrieved from UAV with RMSE 0.0672 was confirmed plausible for water level estimation from flood map generated from SAR images. This was an indication that UAV's DEM is reliable for hydraulic modeling purpose.

4. DISCUSSION

Utilization of Unmanned Aerial Vehicle as known as drone for DEM retrieval have been done in this research, resulted in a protocol on how to generate a DEM from UAV corresponding to the hydraulics modelling purposes. The research was directed in three main constructed milestones as demonstrated in the results; UAV's Image acquisition and processing resulted in the DSM, the conversion of DSM to DEM, and the application of the generated DEM for determining the flood threshold value with flood maps from Sentinel-1 SAR time series imagery. All those processes were applied to inspect the reliability of DEM generated from UAV to be used as a hydraulic modelling main parameter. The results from every main step will be properly discussed for constructing the research to be a valuable contribution specifically for hydraulics and earth science application in general.

4.1. DEM Generation from dense-matched points of UAV Imagery

As indicated that low uncertainties required for the DEM that would be used as the main parameter for hydraulics modelling, this research have applied structured stages to generate the high accuracy DEM. Drone demonstrated very practical tools for photogrammetry data retrieval. Type of drone in accordance with the flying altitude and image overlap percentages were crucially affected the image quality captured, concluded by numbers of previous research. As specified that drone type that was used for this research was a quadcopter type DJI Phantom 4 which apparently effective for capturing relatively small area. The ability to fly at low altitude in "slower" speed flight and big overlap images have produced high-resolution images that gave advantages in the surfaces reconstruction due to accurate tie points and control points spatial recognition. Gafurov (2018) used the same type of drone for DEM retrieval of 2,33 km² small catchment area of the Temev Ruchey river basin, 1.6 km² dry valleys and 0.18 km²of Veduga river basin, and 2.77 km² dry valley of Medveditsa river basin. The research has resulted in a reliable accuracy of the DEM to be used to calculate erosion losses in different part of the temporary network. It is also proved that the DEM generated by this method was applicable for the quantitative and qualitative assessment of gully erosion using the erosion models. Another research conducted by Ajayi, Salubi, Angbas, and Odigure, (2017) have investigated the robustness of DEM generation from the same type of drone that flight at 50 m altitude with very less image overlap, approximately 15-20% and covered nearly 11 ha area. The DEM generated from this research was validated with Differential GPS coordinates and obtained the RMSE for horizontal and vertical accuracy are 0.0270 (x), 0.0467 (y), and 0.1151 (z). The research has also compared the average differences of the heights obtained from DGPS and UAV's DEM is -0.015 m, that quite robust and accurate according to the DEM purpose. The similarity of those two types of research above was the DEMs were generated from a non dominant-vegetated area, in fact, both of the area surfaces were mostly bare land: dry valley in gully area located in Russia (Gafurov, 2018) and bare soil with buildings in Minna, Nigeria. The bare surfaces condition apparently gave a good impact for images calibration that was used for DEM production and also brought advantage for flying low to have a high-resolution image as expected.

Not entirely similar condition has been addressed in this research where flying low at 50 m altitude is given main issues of the un-represented object from the surfaces, specifically above the high-density vegetation. The images were acquired with 80% front and side overlap images, which were considered very proper for stereoscopic view requirement of image matching. However, with this flight specification, there were numbers of uncalibrated images issues that identified above the area of dense vegetation such as trees, scrubs, and maize. The flying altitude 50 m and bigger overlap were designed to acquire a small ground sampling distance which will give a high spatial resolution that later expected to result in a very low uncertainty DEM. However, from this flying height combined with leaves dynamics movement and moving the vehicle at the certain speed, resulted in the tie points from each consecutive images on high-density

vegetation were difficult to detect for an image matching. This occurrence was also addressed by research conducted by Meng et al. (2017) that was utilized the UAV photogrammetric for a terrain mapping in the densely vegetated environment. The research was using a hexacopter drone with flight height 42 m above the ground and overlap 74% front and 55% side overlap, faced a major challenge which is the lack of matching points on the densely vegetated area. The solution on the terrain estimation under this high-density vegetated area modifies the object-oriented classification scheme and assigns a terrain correction factor to each class based on the elevation samples from RTK-GPS measurement. Another research addressed the similar issues on UAV's images coverage above dense vegetation was reported by Mesas-Carrascosa et al. (2015) and Hird et al. (2017) who concluded multiple flights with different heights as a solution, which are 60 m, 80 m, to 100 m (Mesas-Carrascosa et al., 2015) and 58 m to 75 m (Hird et al., 2017). Numbers and distribution of GCP were also modified according to the changing of the flying height, the size of the area to be covered, and the land covers type (adding more GCPs at the densely vegetated area). From multiple times of flights height with modification on numbers of distribution of GCPs, there was a variety of the data quality available that were given the advantages to overcome the issue. Niederheiser et al. (2018) applied multiple times of oblique view images from different heights to added the nadir view images that were processed. Oblique view images that were added giving a significant improvement on the surface reconstruction that effectively affected the point cloud quality so that clearer classification of the land surface's object could be applied. Later was ground and non-ground objects could be distinguished successfully with the method. Multiple time oblique view images proved more comprehensive technique even though this method could be very time-consuming in image processing.

It is noted that the point cloud density and correct cloud points classification extremely affected the quality of the terrain reconstruction result. Dense point cloud generated from aerial photogrammetry (in this case from UAV) only could be occurred by numbers of matching tie points that were assembled from overlap calibrated consecutive images. Realising the concept and considering to improve the quality of the data owned from the first flight on 15 September 2017, two re-flights at the research area were conducted. The second flight was directed on 22 September 2017 which was planned to cover a wider area and added more flights with higher altitude, apparently not succeed due to lack of technical preparation on batteries back-up. The third flight was planned by hired outsource company on 2 November 2017 and flew at 80m altitude, nevertheless neither succeed and resulted in none of the images was stored. Eventually, the research was continued with all the circumstances and the data quality which were retained.

As stated in the research question that the influences of numbers and distribution of Ground Control Points (GCP) will be addressed, then the influences were founded not exactly the same between GCPs for image orientation/georeferencing purpose and the validation of produced DEMs. Based on the DSM and Orthophoto resulted, evenly distributed GCPs on the area have generated a true oriented georeferenced spatial products. There are 7 GCPs used for georeferencing, assessed with mean RMS Error 0.033 for 3D (overall) accuracy, and specifically 0.026 in X direction, 0.022 in Y direction, and 0.053 in Z direction. This result indicated that small numbers of GCPs along the area still produced in a high accuracy georeferenced product due to the evenly distributed position. GCP's used for image georeferenced was an important substance for high-density point cloud generation. Referring to that purpose, it needs to be considered to have GCPs distributed on the different land covers, especially on the object with vary density such as high vegetation/trees, shrubs, agricultural crops, high grass, and other dense vegetation. Added GCP this way would increase the density of the point cloud generated from UAV images (Hird et al., 2017). On the other hand, the validation the Z coordinate (elevation) of UAV's DEM not only required an equally distributed but also needed as many as possible of the GCPs as the reference. As addressed that GCP points were measured with vertical accuracy 15 mm + 0.5 ppm RTK-DGPS method, means that from frequent numbers of manufacture testing with vary condition as many as possible, the instrument measurement have vertically

15mm floating around on every measurement and 0.5 Part Per Million (PPM) means extra 0.5mm error for every kilometer of the rover away from the base. The measurements were done with 34 GCPs; 15 points left bank and 19 points right bank along the river banks that were covered in UAV's flight images. The numbers of GCPs used was numerous compared to GCPs used for georeferenced, which was reasonable to validate the elevation of DEM generated, as such it will be reliable to be used. Numbers of GCPs affected significantly for validation of a DEM generated from UAV, and also addressed in a comprehensive research conducted by Rock, Ries, and Udelhoven (2011). The research has collected 1042 GCPs and used aerotriangulation to investigate the effect on numbers of GCP to external orientation accuracy which stated the accuracy of the elevation (heights) in DEM generated. The research concluded that the RMSE value decreased as numbers of GCPs were added.

4.2. Assessment Accuracy of UAV's DEM generated

DEM generated from this research showed reliable result based on the validation with the reference point from DGPS measurement. RMSE values of 0.0617 for 2cm resolution and 0.0522 for 40cm DEM resolution compared with reference points have gained from the DEM set produced by modification on ground filtering parameter. The validation result of UAV's DEM with reference were compared to the validation result of AHN2 DEM with the reference, as noticed that AHN2 DEM is a reliable terrain platform used by Waterschap and Rijkswaterstaat of The Netherlands. Based on this comparison, the UAV's DEM created from the research showing a comparable performance and considered as acceptable be used further for water level estimation. Clearly noted from validation that RMSE value has reduced from DEM generated by "extra fine nature" default algorithm and after the DEM re-generated with modified every single filtering parameter: *step, bulge, spike, offset,* and *standard deviation*. Modifying the filtering parameters (step, bulge, spike, offset, and standard deviation) clearly improved the quality of the DEM compared the default algorithm, despite it is very time-consuming.

From the research, it is known that every filtering parameter affected differently to DEM, meaning that none of the parameter set provided the same responses from all the reference points. There is always one or two points that respond differently or even opposite with the others which have similar responses. Noticed that two major influence factor of DEM conversion accuracy were the land cover and the slope, this research has indicated that points under the high trees/shrubs and at the steeper slope given bigger deviation compare with others. These challenges were required different approachment of ground filtering on each reference points. This fact has supported the decision on not using the default filtering parameter (fine, extra fine, and ultra-fine) for retrieving the robust DEM set, particularly for hydraulics modelling purposes due to "generalisation" effect when converting to terrain model.

4.3. Flood Water Level Determination from SAR Imagery

SAR images application for flood detection have been applied in this research, utilised the Sentinel-1 images generated the water level measurement on the flood event. As addressed that SAR images application for flood detection, prominent approachment produced a dependable result on water level estimation combined with DEM retrieved from UAV. SAR Images utility was highly reliable even though it was not straightforward. It required a comprehensive analysis in well-structured phases on the images processing according to the research objective. Image processing on SAR images for flood map generation in this research was applied in main stages; geometric correction, stated the image polarisation type used, image filtering and estimation of flood water extent by threshold determination on the image backscatter value.

Noticed that side looking of SAR images compound with rugged topography induced the distortions on the images, so the images were later geometrically corrected with range-doppler terrain correction to moves the image pixels into correct spatial orientation. Terrain correction was a standard procedure and required in

science application of SAR images before further image analysis applied. There were at least 431 Sentinel-1 images from 2014 to 2017 were terrain corrected in this research. The excessive numbers of SAR images was required for a comprehensive study on time series analysis for flood monitoring and mitigation purposes (Martinis, Fissmer, & Rieke, 2015; Ouled Sghaier et al., 2018; Rahman & Thakur, 2017). Terrain corrected images were later converted to decibel of VH (cross polarisation) and VV (single polarisation) band from each image, to distinguish the flood water extraction from the image. There were different points of view in which polarisation was more effective to extract water bodies based on the literature. VH polarisation for water bodies extraction has demonstrated better potential to differentiate water bodies by designated threshold values very well located in the histogram valleys of every performed algorithm (Duy, 2016). Cross-polarization of VH was addressed very well performed of wind speed retrieval on the ocean surfaces occurred under the wind condition that affected the water surface roughness (Huang, Liu, Li, Zhang, & Yu, 2017). Another literature has confirmed multi-polarization resulted in prominent result on water bodies detection where every image polarisation used (HH, VV, and HV) have performed the optimum water classification with variable threshold range for each different polarisation (Manjusree, Prasanna Kumar, Bhatt, Rao, & Bhanumurthy, 2012b). However, this research has proved that using VV polarisation on flood water detection produced a robust result. Visually comparing images of different polarisation in db bands, was confidently shown that water bodies reflected more distinguished in the images. The contrast differences on flood water bodies and the land observed from the flooded event images were very clear as presented on the result. Decision on using VV polarisation also supported by the research evidences on similar investigations that VV demonstrated fewer misclassifications (Clement et al., 2017), presented higher contrast between land and water (Čotar et al., 2016) and proved a slightly higher thematic accuracies on water bodies extraction under calm wind condition (Twele et al., 2016).

Next crucial steps in flood water detection were the image filtering that was applied integrated with the threshold value for flood water distinguishing. Image filtering and backscatter threshold delimitation in band math was always applied in sequences. The changes that was implied on image filtering have always confirmed with the visual assessment on the threshold valued images where the flooded looks reasonable or not. Numbers of trials with different set of filtering and backscatter value inputs have resulted the 5x5 kernel size speckle filtering and -15 db VV band flood threshold value was used for every flood image. The method of retrieving the threshold value to distinguish between the permanent water bodies and flood water with colour composite was also found very effective. This method could reduce the number of "trials values" that were potentially tested and save time. The potential threshold values were limited to certain numbers, then applied to the image before stated the threshold backscatter value that was valid for all images. The applied method for band math filtering was a critical part of the methodology, in order to automize the processing, using the same filtering and backscatter threshold value for all 46 flood images.

There are 46 flood maps generated from SAR time series images, using the UAV's DEM result in the flood frequency map. Flood frequency map indicated the frequencies of inundation occurred around the area included the water level in-situ measurement. Based on this information, the validation of water level measured from in-situ and with UAV's DEM application could be done. This validation was necessary: In this way it could be tested whether the flood maps estimated from SAR and the high-resolution DEM were reliable. Apparently, the validation was applied only at Zoekerbrug station which found reasonable due to data completeness on both side; in-situ measurement and the evidence of the area have been flooded or not in the same particular date/time. Promising results on the water bodies extracted from SAR images and water levels measured on the UAV's DEM with the relation to the in-situ measurement from the validation, have demonstrated that the method proposed in the research objective was plausible.

5. CONCLUSION

The number and distribution of Ground Control Points (GCP) critically affected the image orientation/georeferenced of the UAV images. Sufficient number and evenly distribution of the GCPs were proved positively impacting the DSM reconstruction of the photogrammetry based products. As the tie points, GCPs required being measured by high accuracy method to ensure the quality of oriented images. In this research, the small numbers of GCPs were used for georeferencing the images retrieved from UAV flights, resulted in reliable georeferenced images as indicated with acceptable Root Mean Square Error (RMSE) value. This has proved that evenly distributed GCP's were significantly impacting the image orientation than GCPs in quantities. However, for the point cloud generation, number of GCPs placed/taken from diverse land and topography were indicated required. This was addressed due to uncalibrated images issue that was obtained above the high-density vegetation where there were not GCPs placed.

The most important steps in DSM to DEM conversion process was the ground class filtering. This was the step where the correct ground class extracted and later converted as the terrain. In principle, point cloud that was constructed from the stereoscopic view of UAV images could generate a high accuracy terrain model, which is proved from this research. However, modification of filtering parameter was required to be addressed differently by numbers of customisations on each filter parameter. A structured process that was applied through this research has resulted in a reliable DEM based on the validation with RTK-GPS reference points. This indicated that this research had produced a robust protocol of DEM generation from UAV for hydraulic modelling purposes.

Utilized UAV's DEM combined with flood maps from SAR imagery for water level estimation were done in this research, resulting in comparable water level measured from UAV's DEM compared to in-situ measurement data as the reference. UAV's DEM have indicated reliability to be used effectively for flood water extent mapping in a flooded area where topography data availability was an issue so that terrain data retrieved with UAV could be a practical solution and time-efficient.

5.1. Limitations

Even though the research was conducted in a structured process resulted in dependable products, few numbers of limitation were considered from this research :

1. The fact that uncalibrated images that were consequences some of "blank" area on the point cloud/DSM generated were affected the validation objects range of the DEM. Fully covered DSM will be an advantage on the validation of the UAV's DEM at different object areas such as middle vegetation, high vegetation, buildings, and another different land cover.
2. There were numbers of incomplete in-situ measurement data that were affected by the numbers of water level samples that might contribute the validation of SAR imagery water level and in-situ water level measurement as the reference.

5.2. Recommendation

1. The possibilities of further studies on applications of UAV for high accuracy DEM retrieval for hydraulics modeling purpose. The study that can be addressed on a different type of drone, higher flight height above the vegetated area, differ image acquisition views; nadir and oblique, and cross flight pattern in addition to linear pattern. Investigations on the influence of those parameter are potentially developed for more comprehensive DEM generation especially for dense-matched photogrammetry data source in order to support hydraulics/hydrodynamics application purposes in the future.
2. Further inspection on the effect of filtering parameters at DSM to DEM conversion; step, bulge, spike, offset, and the standard deviation are required. Comprehensive studies on each parameter influence at vary condition as possible will be very valuable for DSM to DEM filtering conversion in future. The inspection will recommend which parameter is most and less sensitive contributed to generated DEM.
3. Similar to filtering parameter modification on the DEM generation, further inspection on Sentinel-1 SAR imagery polarisations used for the optimum water extent extraction among different condition with more complex neighbourhood also recommended to be applied.

LIST OF REFERENCES

Ajayi, O. G., Salubi, A. A., Angbas, A. F., & Odigure, M. G. (2017). Generation of accurate digital elevation models from UAV acquired low percentage overlapping images. *International Journal of Remote Sensing*, 1–22. https://doi.org/10.1080/01431161.2017.1285085

Altenau, E. H., Pavelsky, T. M., Moller, D., Lion, C., Pitcher, L. H., Allen, G. H., … Smith, L. C. (2017). AirSWOT measurements of river water surface elevation and slope: Tanana River, AK. *Geophysical Research Letters*, *44*(1), 181–189. https://doi.org/10.1002/2016GL071577

American Society for Photogrammetry and Remote Sensing. (2011). LASer (LAS) File Format Exchange Activities – ASPRS. Retrieved December 31, 2017, from https://www.asprs.org/committee-general/laser-las-file-format-exchange-activities.html

Amitrano, D., Martino, G., Iodice, A., Mitidieri, F., Papa, M., Riccio, D., & Ruello, G. (2014). Sentinel-1 for Monitoring Reservoirs: A Performance Analysis. *Remote Sensing*, *6*(12), 10676–10693. https://doi.org/10.3390/rs61110676

Béjar-Pizarro, M., Notti, D., Mateos, R. M., Ezquerro, P., Centolanza, G., Herrera, G., … Fernández, J. (2017). Mapping Vulnerable Urban Areas Affected by Slow-Moving Landslides Using Sentinel-1 InSAR Data. *Remote Sensing*, *9*(9), 876. https://doi.org/10.3390/rs9090876

Bioresita, F., Puissant, A., Stumpf, A., & Malet, J.-P. (2018). A Method for Automatic and Rapid Mapping of Water Surfaces from Sentinel-1 Imagery. *Remote Sensing*, *10*(2), 217. https://doi.org/10.3390/rs10020217

Brisco, B., Kapfer, M., Hirose, T., Tedford, B., & Liu, J. (2011). Evaluation of C-band polarization diversity and polarimetry for wetland mapping. *Canadian Journal of Remote Sensing*, *37*(1), 82–92. https://doi.org/10.5589/m11-017

Cazals, C., Rapinel, S., Frison, P.-L., Bonis, A., Mercier, G., Mallet, C., … Rudant, J.-P. (2016). Mapping and Characterization of Hydrological Dynamics in a Coastal Marsh Using High Temporal Resolution Sentinel-1A Images. *Remote Sensing*, *8*(12), 570. https://doi.org/10.3390/rs8070570

Chandel, R., & Gupta, G. (2013). Image Filtering Algorithms and Techniques: A Review. *International Journal of Advanced Research in Computer Science and Software Engineering*, *3*(10), 2277–128. Retrieved from https://pdfs.semanticscholar.org/acc5/3ba7ec21ff7eab60baf9506747c181012d6f.pdf

Chen, C., Li, Y., Yan, C., Dai, H., & Liu, G. (2015). A Robust Algorithm of Multiquadric Method Based on an Improved Huber Loss Function for Interpolating Remote-Sensing-Derived Elevation Data Sets. *Remote Sensing*, *7*(3), 3347–3371. https://doi.org/10.3390/rs70303347

Clement, M. A., Kilsby, C. G., & Moore, P. (2017). Multi-temporal synthetic aperture radar flood mapping using change detection. *Journal of Flood Risk Management*. https://doi.org/10.1111/jfr3.12303

Čotar, K., Oštir, K., & Kokalj, Ž. (2016). RADAR SATELLITE IMAGERY AND AUTOMATIC DETECTION OF WATER BODIES RADARSKI SATELITSKI SNIMCI I AUTOMATSKO OTKRIVANJE VODENIH POVRŠINA. *Geodetski Glasnik*, *50*(47), 5–15. Retrieved from http://www.suggsbih.ba/GEODETSKI GLASNIK/GEODETSKI_GLASNIK_47/GG47_Cotar_Ostir_Kokalj.pdf

Drever, J. I. (2005). *Surface and ground water, weathering, and soils*. Elsevier.

Dunne, T., & Black, R. D. (1970). Partial Area Contributions to Storm Runoff in a Small New England Watershed. *Water Resources Research*, *6*(5), 1296–1311. https://doi.org/10.1029/WR006i005p01296

Duy, N. B. (2016). Automatic detection of surface water bodies from Sentinel-1 SAR images using Valley-Emphasis method. *VIETNAM JOURNAL OF EARTH SCIENCES*, *37*(4). https://doi.org/10.15625/0866-7187/37/4/8298

ESA. (2010). Image Processing with Next ESA SAR Toolbox (NEST) Flood Mapping Using ASAR Data with NEST. Retrieved from http://earth.eo.esa.int/download/eoedu/Earthnet-website-material/to-access-from-Earthnet/2010_AndeSAT-practical-sessions_Bolivia/ASAR-Ecuador-floods.zip

Gafurov, A. M. (2018). Small catchments DEM creation using Unmanned Aerial Vehicles. *IOP Conference Series: Earth and Environmental Science*, *107*, 12005. https://doi.org/10.1088/1755-1315/107/1/012005

Giustarini, L., Vernieuwe, H., Verwaeren, J., Chini, M., Hostache, R., Matgen, P., … De Baets, B. (2015). Accounting for image uncertainty in SAR-based flood mapping. *International Journal of Applied Earth Observation and Geoinformation*, *34*, 70–77. https://doi.org/10.1016/J.JAG.2014.06.017

Greifeneder, F., Wagner, W., Sabel, D., & Naeimi, V. (2014). Suitability of SAR imagery for automatic flood mapping in the Lower Mekong Basin. *International Journal of Remote Sensing*, *35*(8), 2857–2874.

https://doi.org/10.1080/01431161.2014.890299
Grimaldi, S., Li, Y., Pauwels, V. R. N., & Walker, J. P. (2016). Remote Sensing-Derived Water Extent and Level to Constrain Hydraulic Flood Forecasting Models: Opportunities and Challenges. *Surveys in Geophysics*, *37*(5), 977–1034. https://doi.org/10.1007/s10712-016-9378-y
Haala, N., & Cavegn, S. (2016). HIGH DENSITY AERIAL IMAGE MATCHING: STATE-OF-THE-ART AND FUTURE PROSPECTS. *ISPRS - International Archives of the Photogrammetry, Remote Sensing and Spatial Information Sciences*, *XLI-B4*, 625–630. https://doi.org/10.5194/isprsarchives-XLI-B4-625-2016
Haile, A., & Rientjes, T. (2005). Effects of LiDAR DEM resolution in flood modelling: a model sensitivity study for the city of Tegucigalpa, Honduras. *Isprs Wg Iii/3, Iii/4*, 168–173. Retrieved from http://www.isprs.org/proceedings/XXXVI/3-W19/papers/168.pdf
Hird, J. N., Montaghi, A., Mcdermid, G. J., Kariyeva, J., Moorman, B. J., Nielsen, S. E., … Ca, M. (2017). Use of Unmanned Aerial Vehicles for Monitoring Recovery of Forest Vegetation on Petroleum Well Sites. *Remote Sensing*. https://doi.org/10.3390/rs9050413
Hostache, R., Matgen, P., Schumann, G., Puech, C., Hoffmann, L., & Pfister, L. (2009). Water Level Estimation and Reduction of Hydraulic Model Calibration Uncertainties Using Satellite SAR Images of Floods. *IEEE TRANSACTIONS ON GEOSCIENCE AND REMOTE SENSING*. Retrieved from https://pdfs.semanticscholar.org/d00c/7b707d419d8fd7705678a1b32cc04926f235.pdf
Hua, C., Qi, J., Shang, H., Hu, W., & Han, J. (2016). Detection of collapsed buildings with the aerial images captured from UAV. *Science China Information Sciences*, *59*(3), 32102. https://doi.org/10.1007/s11432-015-5341-7
Huang, L., Liu, B., Li, X., Zhang, Z., & Yu, W. (2017). Technical Evaluation of Sentinel-1 IW Mode Cross-Pol Radar Backscattering from the Ocean Surface in Moderate Wind Condition. *Remote Sensing*, *9*(12), 854. https://doi.org/10.3390/rs9080854
Isenburg, M., & Lavy, M. (2017). Removing Excessive Low Noise from Dense-Matching Point Clouds | rapidlasso GmbH. Retrieved February 22, 2018, from https://rapidlasso.com/2017/07/04/removing-excessive-low-noise-from-dense-matching-point-clouds/
Jenson, S. K. (1991). Applications of hydrologic information automatically extracted from digital elevation models. *Hydrological Processes*, *5*(1), 31–44. https://doi.org/10.1002/hyp.3360050104
Judi, D. R., Burian, S. J., & McPherson, T. N. (2011). Two-Dimensional Fast-Response Flood Modeling: Desktop Parallel Computing and Domain Tracking. *Journal of Computing in Civil Engineering*, *25*(3), 184–191. https://doi.org/10.1061/(ASCE)CP.1943-5487.0000064
Kwak, Y., & Young-joo. (2017). Nationwide Flood Monitoring for Disaster Risk Reduction Using Multiple Satellite Data. *ISPRS International Journal of Geo-Information*, *6*(7), 203. https://doi.org/10.3390/ijgi6070203
Lavreniuk, M., Kussul, N., Meretsky, M., Lukin, V., Abramov, S., & Rubel, O. (2017). Impact of SAR Data Filtering on Crop Classification Accuracy. *IEEE First Ukraine Conference on Electrical and Computer Engineering (UKRCON)*. Retrieved from http://inform.ikd.kiev.ua/content/ua/publications/articles/content/2017/Impact of SAR data filtering on crop classification accuracy.pdf
Leica, G. A. G. (2018). Leica Viva GS14 – GNSS Smart Antenna. Retrieved January 22, 2018, from https://leica-geosystems.com/products/gnss-systems/smart-antennas/leica-viva-gs14
Makynen, M., & Karvonen, J. (2017). Incidence Angle Dependence of First-Year Sea Ice Backscattering Coefficient in Sentinel-1 SAR Imagery Over the Kara Sea. *IEEE Transactions on Geoscience and Remote Sensing*, *55*(11), 6170–6181. https://doi.org/10.1109/TGRS.2017.2721981
Manjusree, P., Prasanna Kumar, L., Bhatt, C. M., Rao, G. S., & Bhanumurthy, V. (2012). Optimization of threshold ranges for rapid flood inundation mapping by evaluating backscatter profiles of high incidence angle SAR images. *International Journal of Disaster Risk Science*, *3*(2), 113–122. https://doi.org/10.1007/s13753-012-0011-5
Manjusree, P., Prasanna Kumar, L., Bhatt, C. M., Rao, G. S., & Bhanumurthy, V. (2012). Optimization of threshold ranges for rapid flood inundation mapping by evaluating backscatter profiles of high incidence angle SAR images. *International Journal of Disaster Risk Science*, *3*(2), 113–122. https://doi.org/10.1007/s13753-012-0011-5
Manjusree, P., Prasanna Kumar, L., Mohan Bhatt, C., Srinivasa Rao, G., & Bhanumurthy, V. (2012). Optimization of Threshold Ranges for Rapid Flood Inundation Mapping by Evaluating Backscatter Profiles of High Incidence Angle SAR Images. *Int. J. Disaster Risk Sci*, *3*(2), 113–122.

https://doi.org/10.1007/s13753-012-0011-5

Martinis, S., Fissmer, B., & Rieke, C. (2015). Time series analysis of multi-frequency SAR backscatter and bistatic coherence in the context of flood mapping. In *2015 8th International Workshop on the Analysis of Multitemporal Remote Sensing Images (Multi-Temp)* (pp. 1–4). IEEE. https://doi.org/10.1109/Multi-Temp.2015.7245768

Meng, X., Shang, N., Zhang, X., Li, C., Zhao, K., Qiu, X., & Weeks, E. (2017). Photogrammetric UAV Mapping of Terrain under Dense Coastal Vegetation: An Object-Oriented Classification Ensemble Algorithm for Classification and Terrain Correction. *Remote Sensing*, *9*(12), 1187. https://doi.org/10.3390/rs9111187

Mesas-Carrascosa, F.-J., Torres-Sánchez, J., Clavero-Rumbao, I., García-Ferrer, A., Peña, J.-M., Borra-Serrano, I., & López-Granados, F. (2015). Assessing Optimal Flight Parameters for Generating Accurate Multispectral Orthomosaicks by UAV to Support Site-Specific Crop Management. *Remote Sensing*, *7*(12), 12793–12814. https://doi.org/10.3390/rs71012793

Moore, I. D., Grayson, R. B., & Ladson, A. R. (1991). Digital terrain modelling: A review of hydrological, geomorphological, and biological applications. *Hydrological Processes*, *5*(1), 3–30. https://doi.org/10.1002/hyp.3360050103

Mukolwe, M. M., Baldassarre, G. Di, Werner, M., & Solomatine, D. P. (2014). Flood modelling: parameterisation and inflow uncertainty. *Proceedings of the Institution of Civil Engineers - Water Management*, *167*(1), 51–60. https://doi.org/10.1680/wama.12.00087

Niederheiser, R., Rutzinger, M., Bremer, M., & Wichmann, V. (2018). Dense image matching of terrestrial imagery for deriving high-resolution topographic properties of vegetation locations in alpine terrain. *International Journal of Applied Earth Observation and Geoinformation*, *66*, 146–158. https://doi.org/10.1016/J.JAG.2017.11.011

Ouled Sghaier, M., Hammami, I., Foucher, S., & Lepage, R. (2018). Flood Extent Mapping from Time-Series SAR Images Based on Texture Analysis and Data Fusion. *Remote Sensing*, *10*(2), 237. https://doi.org/10.3390/rs10020237

Papastergios A, Chini M, & Parcharidis I. (2016). SENTINEL-1 DATA TO MAP FLOODED AREAS: THE ROLE OF INSAR COHERENCE AND POLARIMETRIC INFORMATION, 1730–1736. Retrieved from https://ejournals.epublishing.ekt.gr/index.php/geosociety/article/viewFile/11896/11918

Rahman, M. R., & Thakur, P. K. (2017). Detecting, mapping and analysing of flood water propagation using synthetic aperture radar (SAR) satellite data and GIS: A case study from the Kendrapara District of Orissa State of India. *The Egyptian Journal of Remote Sensing and Space Science*. https://doi.org/10.1016/J.EJRS.2017.10.002

Reiu, A., Zalite, K., Kaupo, P., & Phd, V. (2017). Classification of urban areas from Sentinel-1 coherence maps. Retrieved from https://dspace.ut.ee/bitstream/handle/10062/57435/reiu_andy.pdf?sequence=1&isAllowed=y

Remo, J. W. F., Carlson, M., & Pinter, N. (2011). Hydraulic and flood-loss modeling of levee, floodplain, and river management strategies, Middle Mississippi River, USA. https://doi.org/10.1007/s11069-011-9938-x

Reshetyuk, Y., & Mårtensson, S.-G. (2016). Generation of Highly Accurate Digital Elevation Models with Unmanned Aerial Vehicles. *The Photogrammetric Record*, *31*(154), 143–165. https://doi.org/10.1111/phor.12143

Rock, G., Ries, J. B., & Udelhoven, T. (2011). SENSITIVITY ANALYSIS OF UAV-PHOTOGRAMMETRY FOR CREATING DIGITAL ELEVATION MODELS (DEM). Retrieved from https://www.int-arch-photogramm-remote-sens-spatial-inf-sci.net/XXXVIII-1-C22/69/2011/isprsarchives-XXXVIII-1-C22-69-2011.pdf

Saxena, N., & Rathore, N. (2013). A review on speckle noise filtering techniques for SAR Images. *International Journal of Advanced Research in Computer Science and Electronics Engineering*, *2*(2), 2277–9043. Retrieved from https://pdfs.semanticscholar.org/c477/2ff50794fc54a0383512cd1bbda3a5d163cd.pdf

Schumann, G. J.-P., & Moller, D. K. (2015). Microwave remote sensing of flood inundation. *Physics and Chemistry of the Earth, Parts A/B/C*, *83–84*, 84–95. https://doi.org/10.1016/J.PCE.2015.05.002

Tamminga, A., Hugenholtz, C., Eaton, B., & Lapointe, M. (2015). Hyperspatial Remote Sensing of Channel Reach Morphology and Hydraulic Fish Habitat Using an Unmanned Aerial Vehicle (UAV): A First Assessment in the Context of River Research and Management. *River Research and Applications*, *31*(3), 379–391. https://doi.org/10.1002/rra.2743

Tanguy, M., Chokmani, K., Bernier, M., Poulin, J., & Raymond, S. (2017). River flood mapping in urban areas combining Radarsat-2 data and flood return period data. *Remote Sensing of Environment*, *198*, 442–459. https://doi.org/10.1016/J.RSE.2017.06.042

Thomas, I. A., Jordan, P., Shine, O., Fenton, O., Mellander, P.-E., Dunlop, P., & Murphy, P. N. C. (2017). Defining optimal DEM resolutions and point densities for modelling hydrologically sensitive areas in agricultural catchments dominated by microtopography. *International Journal of Applied Earth Observation and Geoinformation*, *54*, 38–52. https://doi.org/10.1016/j.jag.2016.08.012

Twele, A., Cao, W., Plank, S., & Martinis, S. (2016). Sentinel-1-based flood mapping: a fully automated processing chain. *International Journal of Remote Sensing*. https://doi.org/10.1080/01431161.2016.1192304

Ullah, S., Farooq, M., Sarwar, T., Tareen, M. J., & Wahid, M. A. (2016). Flood modeling and simulations using hydrodynamic model and ASTER DEM—A case study of Kalpani River. *Arabian Journal of Geosciences*, *9*(6), 439. https://doi.org/10.1007/s12517-016-2457-z

Uysal, M., Toprak, A. S., & Polat, N. (2015). DEM generation with UAV Photogrammetry and accuracy analysis in Sahitler hill. *Measurement*, *73*, 539–543. https://doi.org/10.1016/j.measurement.2015.06.010

Van Sickle, J. (2001). *GPS for land surveyors*. Ann Arbor Press.

Vechtstromen, W. (2017). Hoog water Dinkel, Regge en Vecht - Vechtstromen. Retrieved February 15, 2018, from https://www.vechtstromen.nl/actueel/nieuws-0/@38047/hoog-water-dinkel/

Wegmüller, U., Santoro, M., & Werner, C. (2013). MULTI-TEMPORAL SAR DATA FILTERING FOR LAND APPLICATIONS. Retrieved from https://ftp.space.dtu.dk/pub/Ioana/papers/s244_1wegm.pdf

Wolfert, H. P. (2001). Geomorphological Change and River Rehabilitation. Retrieved from http://www.therrc.co.uk/pdf/References/GeoC_RR.pdf

Woodrow, K., Lindsay, J. B., & Berg, A. A. (2016). Evaluating DEM conditioning techniques, elevation source data, and grid resolution for field-scale hydrological parameter extraction. *Journal of Hydrology*, *540*, 1022–1029. https://doi.org/10.1016/j.jhydrol.2016.07.018

Zhang, H., Zhang, F., Shi, X., Zeng, C., Shih, D.-S., Yeh, G.-T., & Joswiak, D. R. (2014). Influence of river channel geometry in stream flow modelling and guidelines for field investigation. *Hydrological Processes*, *28*(4), 2630–2638. https://doi.org/10.1002/hyp.9837